Dynamic modeling of the horizontal eddy viscosity coefficient for quasigeostrophic ocean circulation problems

Romit Maulik, Omer San*

School of Mechanical and Aerospace Engineering, Oklahoma State University, Stillwater, OK 74078, USA

Abstract

This paper puts forth a simplified dynamic modeling strategy for the eddy viscosity coefficient parameterized in space and time. The eddy viscosity coefficient is dynamically adjusted to the local structure of the flow using two different nonlinear eddy viscosity functional forms to capture anisotropic dissipation mechanism, namely, (i) the Smagorinsky model using the local strain rate field, and (ii) the Leith model using the gradient of the vorticity field. The proposed models are applied to the one-layer and two-layer wind-driven quasigeostrophic ocean circulation problems, which are standard prototypes of more realistic ocean dynamics. Results show that both models capture the quasi-stationary ocean dynamics and provide the physical level of eddy viscosity distribution without using any a priori estimation. However, it is found that slightly less dissipative results can be obtained by using the dynamic Leith model. Two-layer numerical experiments also reveal that the proposed dynamic models automatically parameterize the subgrid-scale stress terms in each active layer. Furthermore, the proposed scale-aware models dynamically provide higher values of the eddy viscosity for smaller resolutions taking into account the local resolved flow information, and addressing the intimate relationship between the eddy viscosity coefficients and the numerical resolution employed by the quasigeostrophic models.

1. Introduction

There is a growing interest in developing subgrid-scale parameterizations for turbulent geophysical flows arising in planetary atmospheres and oceans [1,4,13,20,24,26,27,36,38,39,44–46,48,50,51,56,75,95]. The specifications of dissipation processes in general circulation models play a crucial role in the dynamics of the large-scale nonlinear motions of geophysical flows demonstrating a great variety of complex multiscale flow patterns. For example, wind-driven quasigeostrophic (QG) ocean circulation problems were studied systematically by varying the horizontal eddy viscosity coefficient as a control parameter [6–8]. These studies clearly showed that different eddy viscosity values

may result in different flow regimes identifying a sequence of attractors, including fixed points (steady states), limit cycles (periodic), tori (quasiperiodic), and strange attractors (chaotic). A sequence of transitions to these states has also been recently investigated by Mishra et al. [63] for solving Kolmogorov flows (i.e., flows driven by a spatially periodic force) in a two-dimensional setting. They identified all possible flow regimes together with their bifurcations using both large and small scale dissipation parameters.

As discussed by Frederiksen et al. [26], the need to parametrize the effects of subgrid-scale eddies is perhaps even more important in general ocean circulation models. The main drivers of ocean circulation are the Earth's rotation and atmospheric winds. The ocean circulation is characterized by large circulation zones, or gyres, which can be identified with the strong, persistent, sub-tropical and sub-polar western boundary currents such as the Gulf Stream [49,90]. Generally, the circulation is clockwise in the Northern Hemisphere and

* Corresponding author.
  E-mail addresses: romit.maulik@okstate.edu (R. Maulik), osan@okstate.edu (O. San).

Table 1
The eddy viscosity coefficients used in quasigeostrophic (QG) ocean models.

Study	Model	Range of ν (m^{2}s^{-1})	Resolution
[12]	One-layer	500–10000	40×80
[29]	One-layer	6000–10000	74×50
[41]	One-layer	330	50×50
[47]	One-layer	300	50×100
[85]	One-layer	1000–6000	49×65
[91]	One-layer	200	120×120
[8]	One-layer	54–1000	129×65
[71]	Two-layer	50	151×151
[6]	Two-layer	100–580	129×65
[7]	Two-layer	400–600	256×256
[7]	Two-layer	800–1600	128×128
[5]	Two-layer	100	512×256
[92]	Two-layer	100	500×500
[70]	Three-layer	300–1600	100×100

counterclockwise in the Southern Hemisphere. These circulation patterns emerge when we average over several years. It has been widely recognized that the ocean circulation models use some sort of ad-hoc eddy viscosity coefficients because the horizontal scale of an ocean basin is much larger than the effective scale for molecular dissipation. As discussed in [83], the development of a rigorous, mathematical understanding and subsequent modeling strategy for dissipation mechanisms is one of the major unsolved problems in physical oceanography. An impractically fine resolution would be necessary if the ocean circulation models were to resolve the full spectra of turbulence down to the Kolmogorov scale. Therefore the first and ultimately simplest approach to the subgrid-scale parametrization in ocean dynamics is the use of a Munk scale resolving constant eddy-viscosity coefficient. The eddy viscosities generally used in the quasigeostrophic ocean models are summarized in Table 1. It can be seen that the amount of eddy viscosity used in the models generally decreases with increasing computational resolution.

On the other hand, the functional Smagorinsky model for approximating the eddy viscosity coefficient from the local flow structures has been one of the most celebrated subgrid-scale models parameterizing eddy viscosity [87], focusing only on dissipating energy at a rate that is physically correct. Increasing the effective viscosity of the system, the approach treats dissipation of kinetic energy at subgrid-scales as analogous to molecular diffusion, where the effects of small scale fluctuations are lumped into a functional eddy viscosity. Since then, large eddy simulation (LES) has been proven to be a promising approach for calculations of complex turbulent flows [9,18,23,28,43,54,61,65,74,78,88], and appears as a natural choice in turbulent geophysical flows [15,21,22,64]. LES models specifically developed for two-dimensional turbulent flows, such as those in the atmosphere and oceans, are relatively scarce [3,14,42,84], at least when compared to the plethora of LES models developed for three-dimensional turbulent flows.

The Smagorinsky model assumes that the eddy viscosity is computed from the resolved strain rate magnitude and char-

acteristic length scales which are assumed to be proportional to the filter width via a Smagorinsky constant. Application of the Smagorinsky model to various engineering and geophysical flow problems has revealed that the constant is not single-valued in literature and varies depending on resolution and flow characteristics. A major advance took place with the development of a dynamic model proposed by Germano et al. [30] in which the Smagorinsky constant is self adaptively determined along with the simulation. Therefore, the constant parameter of the Smagorinsky model, c_S, becomes a dynamic field parameter which adapts to the local field conditions in order to adjust subgrid modeling. Lilly [55] proposed modifications to Germano's dynamic model by deriving a well-posed algebraic expression for the coefficient by using a least-squares method. This has made the dynamic model more stable, making the method more widely applicable in many fields (e.g., see [73] and [61]), including combustion [74], multiphase flows [23], acoustics [96], and simulations of the atmospheric boundary layer [89]. A dynamic global coefficient mixed subgrid-scale eddy viscosity model for large eddy simulation of turbulent flows in complex geometries has been also developed [86,97].

An alternative to the Smagorinsky hypothesis was put forward by Leith [52,53], which was based on the adjustment of artificial dissipation varying with the local gradient of vorticity. The formulation of the eddy viscosity obtained through this hypothesis was seen to be more scale selective due to higher order derivatives in the formulation. Furthermore, it was built on the concept of Kraichnan's forward enstrophy cascade instead of the concept of Kolmogorov's forward energy cascade, which is more applicable to three-dimensional turbulent flows [25]. The Leith formulation has been used in both atmospheric models [10] and ocean models [77]. It must be noted here that there have been some attempts to blend the characteristics of both Smagorinsky (strain rate dependence) and Leith (vorticity gradient dependence) characteristics into hybrid models [60]. The Leith formulation for the nonlinear eddy viscosity can also be applied in the dynamic test filtered framework. This requires the adaptive calculation of a mixing length scale constant that controls the value of the eddy viscosity.

The main objective of this work is to put forth a simplified dynamic eddy viscosity subgrid-scale modeling framework for the scale-aware horizontal eddy viscosity parametrization in large scale geophysical flows. A unified dynamic modeling procedure is developed using both Smagorinsky's and Leith's nonlinear eddy viscosity forms. For modeling mesoscale turbulence in the barotropic and baroclinic circulations, the proposed model is applied to both one-layer and two-layer wind-driven quasigeostrophic ocean circulation problems in the beta-plane, which are standard prototypes of more realistic ocean dynamics. The one-layer experiments in rectangular domain yield four gyres in time mean and have been used to test various classes of turbulence closure models including the alpha [42] and approximate deconvolution [83,84] models. The two-layer experiments, including the first baroclinic mode, have also been used to test subgrid-scale models in

a simple stratified flow setting [83], resulting in a double-gyre structure (cyclonic subpolar and anticyclonic subtropical gyres) in time mean.

The remainder of this paper is organized as follows. Section 2 presents the governing equations for the one-layer and two-layer quasigeostrophic ocean circulation models. The proposed models for the eddy viscosity parametrization are explained in Section 3. Section 4 contains a brief description of numerical methods employed in the present study, including the second-order energy conserving Arakawa scheme for spatial discretization, and the third-order Runge Kutta scheme for the time integration, as well as a fast Poisson solver for kinematic relationship between vorticity and streamfunction. The results of numerical experiments are provided in Section 5 using a set of physical and numerical parameters. Section 6 is devoted to concluding remarks.

2. Quasigeostrophic ocean models

2.1. One-layer model

Studies of wind-driven circulation using an idealized double-gyre wind forcing have played an important role in understanding various aspects of ocean dynamics, including the role of mesoscale eddies and their effect on mean circulation. In this section, following [35,82,84], we present the barotropic vorticity equation (BVE) as a representative one-layer quasigeostrophic ocean model for forced-dissipative large scale ocean circulation problems. More details on the physical mechanism of quasigeostrophic models and various formulations can be found in geophysical fluid dynamics monographs [17,32,58,72,93].

The BVE for one-layer quasigeostrophic (QG1) ocean model can be written as

$$\frac{\partial \omega}{\partial t} + J(\omega, \psi) - \beta \frac{\partial \psi}{\partial x} = \nu_e \nabla^2 \omega + F, \tag{1}$$

where the terms in Eq. (1) account for the local accelerative, convective, rotational, dissipative, and surface forcing effects respectively. In Eq. (1), ω is the kinematic vorticity, the curl of the velocity field, defined as

$$\omega = \frac{\partial v}{\partial x} - \frac{\partial u}{\partial y}, \tag{2}$$

and ψ is refers the velocity streamfunction. The kinematic relationship between the vorticity and stream function yields the following Poisson equation:

$$\nabla^2 \psi = -\omega, \tag{3}$$

where ∇^2 is the two-dimensional Laplacian operator. The flow velocity components are defined by

$$u = \frac{\partial \psi}{\partial y}, \quad v = -\frac{\partial \psi}{\partial x}. \tag{4}$$

The BVE given by Eq. (1) uses the beta-plane approximation, which is valid for most of the mid-latitude simplified ocean basins. To account for the Earth's rotational effects,

using Taylor series expansion, in the beta-plane approximation the Coriolis parameter is approximated by $f = f_0 + \beta y$, where f_0 is the constant mean Coriolis parameter at the basin center and β is the gradient of the Coriolis parameter (i.e., $\beta = \partial f / \partial y$) at the same location. The convection term in Eq. (1), called the nonlinear Jacobian, is defined as

$$J(\omega, \psi) = \frac{\partial \psi}{\partial y} \frac{\partial \omega}{\partial x} - \frac{\partial \psi}{\partial x} \frac{\partial \omega}{\partial y}. \tag{5}$$

The viscous dissipation mechanism has the conventional Laplacian form, $\nu_e \nabla^2 \omega$, where ν_e is the horizontal eddy viscosity coefficient for the ocean basin. In the oceans, there exists a whole range of physical processes between the mesoscopic quasigeostrophic scales and the characteristic scale typical of molecular diffusion. These intermediate scales include vertical mixing effects, e.g. associated with wave breaking process which require a separate parameterization. As discussed in [83] and references therein, quasigeostrophic ocean models use eddy viscosity coefficients on the order of 100 m²/s which are many orders of magnitude greater than the molecular viscosity of the sea water (i.e., $\nu = 10^{-6}$ m²/s). This parametrization is used because the horizontal scale of the ocean basin is much larger than the effective scale for molecular diffusion. Therefore an impractically fine resolution would be necessary if the ocean models were to resolve the full spectra of turbulence down to the molecular dissipation scale. On the other hand, the eddy viscosity parameterization used in the quasigeostrophic models plays an important role in the dynamics of the problem. For example, the study of Berloff and McWilliams [7] clearly shows that the use of different values of eddy viscosity results in different dynamics of the quasigeostrophic ocean models ranging from an asymmetric steady state to a chaotic variability. One of the main goals in the present study is to develop a dynamic procedure to compute the eddy viscosity coefficient during the simulation. The following section is devoted to the development of this procedure.

The double-gyre wind forcing function in the model is given by

$$F = \frac{1}{\rho H} \hat{k} \cdot \nabla \times \vec{\tau}, \tag{6}$$

where ρ is the mean fluid density, and H is the mean depth of the ocean basin, and $\vec{\tau}$ refers the stress vector for the surface wind forcing, and $\hat{k}$ is unit vector in vertical direction. In the equation above, ∇ is the gradient operator. In the present model, we use a double-gyre wind forcing only for zonal direction: $\vec{\tau} = (\tau_0 \cos(\pi y/L), 0)$, where L is the meridional length of the ocean basin centered at $y = 0$, and τ_0 is the maximum amplitude of the wind stress. This form of wind stress represents the meridional profile of easterly trade winds, mid-latitude westerlies, and polar easterlies from South to North over the ocean basin [83]. Taking the curl of the stress field, the forcing term can be written as

$$F = \frac{\tau_0}{\rho H} \frac{\pi}{L} \sin\left(\pi \frac{y}{L}\right). \tag{7}$$

In order to obtain a dimensionless form of the BVE, we use the following definitions:

$$\tilde{x} = \frac{x}{L}, \quad \tilde{y} = \frac{y}{L}, \quad \tilde{t} = \frac{t}{L/V}, \quad \tilde{\omega} = \frac{\omega}{V/L}, \quad \tilde{\psi} = \frac{\psi}{VL}, \quad (8)$$

where the tilde denotes the corresponding nondimensional variables. In the nondimensionalization, L represents the characteristic horizontal length scale (in our study L is the basin dimension in the x direction), and V is the characteristic Sverdrup velocity scale given by the following definition:

$$V = \frac{\tau_0}{\rho H} \frac{\pi}{\beta L}. \quad (9)$$

The dimensionless governing equations for the two-dimensional single-layer quasigeostrophic ocean model can be written as

$$\frac{\partial \omega}{\partial t} + J(\omega, \psi) - \frac{1}{\text{Ro}} \frac{\partial \psi}{\partial x} = A \nabla^2 \omega + \frac{1}{\text{Ro}} \sin(\pi y), \quad (10)$$

where we omit the tilde over the variables for the purpose of clarity. Due to the nondimensionalization given by Eq. (8), the kinematic relationship given in Eq. (3) and definition of nonlinear Jacobian given in Eq. (5) remain the same. In the dimensionless form given in Eq. (10), Ro and A control quasigeostrophic ocean dynamics. Referred to respectively as the Rossby and inverse Reynolds numbers they are related to the physical parameters in the following way

$$A = \frac{\nu_e}{VL}, \quad \text{Ro} = \frac{V}{\beta L^2}, \quad (11)$$

where A is the dimensionless eddy viscosity coefficient. The Ro number can be related to the Rhines scale, $\delta_I/L = \sqrt{\text{Ro}}$, which measures the strength of the nonlinearity.

In order to completely specify the mathematical model, boundary and initial conditions need to be prescribed. In many theoretical studies of large scale ocean circulation models, slip or no-slip boundary conditions are used in simplified Cartesian oceanic basins. Following [16,35,42,71,82–84], we use slip boundary conditions for the velocity, which translate into homogeneous Dirichlet boundary conditions for the vorticity: $\omega|_\Gamma = 0$, where Γ symbolizes all the Cartesian boundaries. The corresponding impermeability boundary condition is imposed as $\psi|_\Gamma = 0$. For the initial condition, we start our computations from a quiescent state and solve Eq. (10) numerically until we obtain a statistically steady state in which the wind forcing, dissipation, and nonlinear interactions balance each other. The schematic for the one-layer QG model is provided in Fig. (1).

2.2. Two-layer model

In reality, the ocean is a stratified fluid on a rotating Earth driven from its upper surface by patterns of momentum and buoyancy fluxes [57]. While the one-layer quasigeostrophic model (also known as the barotropic model) is not stratified, it exhibits many of the features observed in the stratified case. The two-layer model adds the effect of stratification through the use of a second dynamically active layer [5,7,19,40,71].
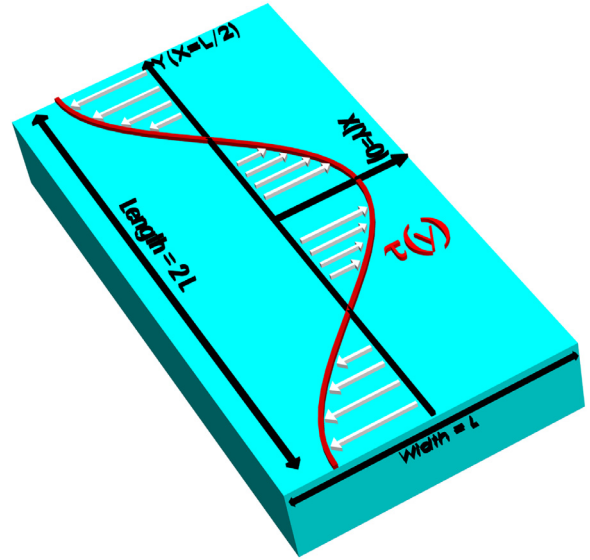

Fig. 1. Schematic for the one-layer quasigeostrophic model with a rectangular ocean basin.

We remark that the complexity of QG models may be enhanced by adding more active layers to get N-layer models [58].

The two-layer quasigeostrophic (QG2) model used in this study is a simplified forced-dissipative model that considers baroclinic effects. The stratified ocean is partitioned into two isopycnal layers with each having the identical depth, density and temperature. The governing equations of the QG2 model are given by

$$\frac{\partial \omega_1}{\partial t} + J(\omega_1, \psi_1) - \beta \frac{\partial \psi_1}{\partial x} = \nu_e \nabla^2 \omega_1 + F_1$$
$$\frac{\partial \omega_2}{\partial t} + J(\omega_2, \psi_2) - \beta \frac{\partial \psi_2}{\partial x} = \nu_e \nabla^2 \omega_2 + F_2, \quad (12)$$

with the isopycnal flow velocity components obtainable through the use of the velocity streamfunction relationship:

$$u_i = \frac{\partial \psi_i}{\partial y}; \quad v_i = -\frac{\partial \psi_i}{\partial x}. \quad (13)$$

where the forcing terms are given by F_1 (for the upper layer) and F_2 (for the bottom layer) where

$$F_1 = \frac{1}{\rho_1 H_1} \hat{k}. \nabla \times \vec{\tau} \quad (14)$$

is the forcing generated due to the stress vector for surface wind as explained in the one-layer formulation. More specifically, in the present two-layer experiments, we use a double-gyre wind forcing only for zonal direction: $\vec{\tau} = (\tau_0 \cos(2\pi y/L), 0)$, where L is the meridional length of the ocean basin centered at $y = 0$. Therefore, the characteristic Sverdrup velocity scale is given by the following definition:

$$V = \frac{\tau_0}{\rho_1 H_1} \frac{2\pi}{\beta L}. \quad (15)$$

The forcing of the bottom layer is given by

$$F_2 = \gamma \nabla^2 \psi_2, \quad (16)$$

where γ is a coefficient of the linear bottom friction which parameterizes the bottom Ekman layer. The vorticity fields for each layer are related to the velocity stream functions through the following elliptic coupled system of equations:

$$\omega_1 = -\nabla^2\psi_1 - \frac{f_0^2}{g'H_1}(\psi_2 - \psi_1)$$
$$\omega_2 = -\nabla^2\psi_2 - \frac{f_0^2}{g'H_2}(\psi_1 - \psi_2) \qquad (17)$$

where H_1 and H_2 are the depths of the individual layers, $g' = g\Delta\rho/\rho_1$ is the reduced gravity associated with the density jump between the two layers in which $\Delta\rho$ is the density difference between the two layers and ρ_1 is the upper layer density. Other relevant symbols have been defined previously. Following a similar process of non-dimensionalization as shown in the previous subsection, we can obtain the dimensionless governing equations of the QG2 model given by

$$\frac{\partial\omega_1}{\partial t} + J(\omega_1, \psi_1) - \frac{1}{\mathrm{Ro}}\frac{\partial\psi_1}{\partial x} = A\nabla^2\omega_1 + \frac{1}{\mathrm{Ro}}\sin 2\pi y$$
$$\frac{\partial\omega_2}{\partial t} + J(\omega_2, \psi_2) - \frac{1}{\mathrm{Ro}}\frac{\partial\psi_2}{\partial x} = A\nabla^2\omega_2 - \sigma\nabla^2\psi_2 \qquad (18)$$

where we define two additional nondimensional quantities, the Froude number (Fr) and σ which is the Ekman bottom layer friction coefficient

$$\mathrm{Fr} = \frac{f_0^2 V}{g'\beta H}; \quad \sigma = \frac{\gamma}{V/L}. \qquad (19)$$

The coupled elliptic equations can also be represented in a nondimensional fashion:

$$\omega_1 = -\nabla^2\psi_1 - \frac{\mathrm{Fr}}{\delta\mathrm{Ro}}(\psi_2 - \psi_1)$$
$$\omega_2 = -\nabla^2\psi_2 - \frac{\mathrm{Fr}}{(1-\delta)\mathrm{Ro}}(\psi_1 - \psi_2) \qquad (20)$$

where $\delta = H_1/H$ and $H = H_1 + H_2$.

To complete the QG2 formulation to be used in this investigation, we prescribe the following initial and boundary conditions. It is a common practice to either use free-slip or no-slip boundary conditions. We follow the studies in [16,71,83] and prescribe free-slip boundary conditions for the velocity for both isopycnal layers which manifest in the form of homogeneous Dirichlet boundary conditions for the vorticity (Laplacian of streamfunction): $\nabla^2\psi|_\Gamma = 0$. An impermeability boundary condition is imposed by forcing $\psi|_\Gamma = 0$. We start from a quiescent state and integrate till a statistically steady state is obtained and continue for several decades to compute time-averaged results. The schematic for the two-layer QG model is provided in Fig. (2).

3. Dynamic eddy viscosity parametrization

The first and ultimately simplest approach to the eddy viscosity parametrization is the use of a Munk scale resolving constant eddy-viscosity coefficient in the model (e.g., see Table 1). An improved approach is called as functional eddy viscosity modeling which parametrizes eddy viscosity through
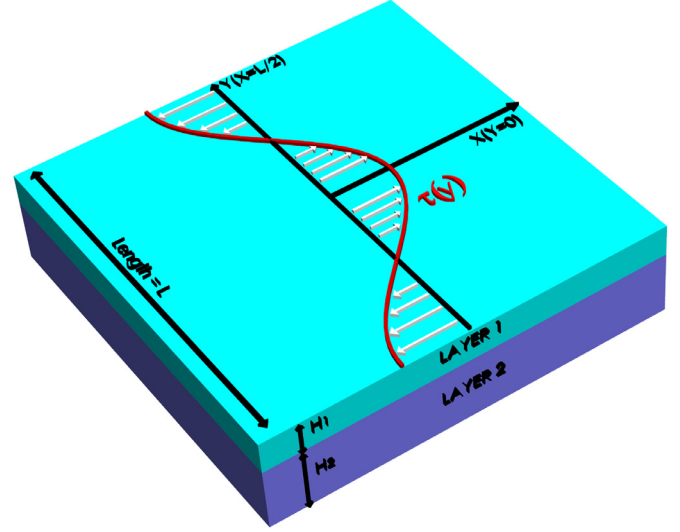

Fig. 2. Schematic for the two-layer quasigeostrophic model with a square ocean basin.

using a functional relationship between the eddy viscosity distribution and the resolved flow dynamics.

3.1. Smagorinsky hypothesis

One of the most popular functional eddy viscosity parametrizations is called the Smagorinsky model which assumes that the eddy viscosity coefficient is proportional to the absolute strain rate [87]. The tensorially invariant Smagorinsky model is written as

$$\nu_e = \ell_0^2 |S|, \qquad (21)$$

where ℓ_0 is the mixing length scale, and $|S| = \sqrt{2S_{ij}S_{ij}}$ is the absolute value of the strain rate tensor given by

$$S_{ij} = \frac{1}{2}\left(\frac{\partial u_i}{\partial x_j} + \frac{\partial u_j}{\partial x_i}\right), \qquad (22)$$

where u_i is the ith velocity component along x_i direction. This model has been primarily used as a subgrid-scale model for large eddy simulation (LES) of turbulent flows and needs for an ad hoc specification of ℓ_0, a task that is all but impossible in any functional subgrid-scale parametrization. In two dimensional settings (i.e., $u_1 = u$ and $u_2 = v$), the absolute strain rate field is given as

$$|S| = \sqrt{\left(\frac{\partial u}{\partial y} + \frac{\partial v}{\partial x}\right)^2 + 2\left(\frac{\partial u}{\partial x}\right)^2 + 2\left(\frac{\partial v}{\partial y}\right)^2}, \qquad (23)$$

or in terms of the streamfunction it can be written as

$$|S| = \sqrt{4\left(\frac{\partial^2\psi}{\partial x\partial y}\right)^2 + \left(\frac{\partial^2\psi}{\partial x^2} - \frac{\partial^2\psi}{\partial y^2}\right)^2}. \qquad (24)$$

Using Eqs. (21) and (24), the horizontal eddy viscosity coefficient can be parameterized as

$$\nu_e = c_S^2\delta^2\sqrt{4\left(\frac{\partial^2\psi}{\partial x\partial y}\right)^2 + \left(\frac{\partial^2\psi}{\partial x^2} - \frac{\partial^2\psi}{\partial y^2}\right)^2} \qquad (25)$$

in which the mixing length scale ℓ_0 is parameterized by using the well-known Smagorinsky constant (i.e., $\ell_0 = c_S \delta$). In Eq. (25), c_S is the Smagorinsky constant and depends on the physics of the flows (i.e., usually reported between 0.1 and 0.2 in the LES literature), and δ is the characteristic length scale representing the computational resolution (i.e., $\delta^2 = \Delta x \Delta y$ where Δx and Δy are the mesh size for the numerical discretization in x- and y-directions).

3.2. Leith hypothesis

The other alternative in terms of a nonlinear viscosity kernel is the use of Leith viscosity based on the local gradient of vorticity to account for a forward enstrophy cascade [52]. An expression for the Leith model can be derived in a manner similar to the Smagorinsky viscosity to give

$$\nu_e = c_L^3 \delta^3 |\nabla \omega| \tag{26}$$

where

$$|\nabla \omega| = \sqrt{\left(\frac{\partial \omega}{\partial x}\right)^2 + \left(\frac{\partial \omega}{\partial y}\right)^2}. \tag{27}$$

As mentioned previously, the gradient of vorticity imparts an increased scale-aware characteristic to the viscosity kernel leading to improved dissipation characteristics in turbulent regions of the flow. The prefactor c_L behaves in a similar manner to the Smagorinsky coefficient c_S and can be specified prior to the simulation or calculated dynamically as elucidated below.

3.3. Dynamic approximation of model constants

The specified value of c_S or c_L plays an important role of the dissipation dynamics of the problems and turns out different optimal values for different flow regimes and computational resolutions. A dynamic procedure to compute c_S has been proposed by Germano et al. [30] and Lilly [55] proposed modifications to Germano's dynamic model by deriving a well-posed algebraic expression for the coefficient by using a least-squares method, which has successfully been applied to a number of turbulent flows (e.g., see [61,73]). Since then various forms of the dynamic model have also been reported for LES computations [31,89,97]. In the following, proceeding according to San [80] a simplified dynamic modeling framework for computing c_S and c_L in Eqs. (25) and (26), respectively, is derived for the quasigeostrophic ocean model governed by the barotropic vorticity equation given by Eq. (1). Without losing generality, the extension to the QG2 formulation and other variants of quasigeostrophic ocean models is straightforward.

Using the eddy viscosity hypothesis, the nondimensional governing equations for the QG model reads

$$\frac{\partial \omega}{\partial t} + J(\omega, \psi) - \beta \frac{\partial \psi}{\partial x} = c_S^2 \delta^2 |S| \nabla^2 \omega + \frac{1}{\text{Ro}} \sin \pi y \tag{28}$$

where δ refers the grid scale. Without loss of generality, Eq. (28) can be rewritten for the test filtered scale as follows

$$\frac{\partial \overline{\omega}}{\partial t} + J(\overline{\omega}, \overline{\psi}) - \beta \frac{\partial \overline{\psi}}{\partial x} = c_S^2 \overline{\delta}^2 |\overline{S}| \nabla^2 \overline{\omega} + \frac{1}{\text{Ro}} \sin \pi \overline{y} \tag{29}$$

where the superscript over bar refers the test filtered scale (i.e., $\overline{\delta} > \delta$). We note that the filtering process commutes with the differentiation operators. Applying the same test filter to Eq. (28) yields

$$\frac{\partial \overline{\omega}}{\partial t} + \overline{J(\omega, \psi)} - \beta \frac{\partial \overline{\psi}}{\partial x} = c_S^2 \delta^2 \overline{|S| \nabla^2 \omega} + \frac{1}{\text{Ro}} \sin \pi \overline{y}, \tag{30}$$

and the result is subtracted from Eq. (29), leading to

$$J(\overline{\omega}, \overline{\psi}) - \overline{J(\omega, \psi)} = c_S^2 \overline{\delta}^2 |\overline{S}| \nabla^2 \overline{\omega} - c_S^2 \delta^2 \overline{|S| \nabla^2 \omega}, \tag{31}$$

which may be simplified to

$$L = (c_S \delta)^2 M \tag{32}$$

where

$$L = J(\overline{\omega}, \overline{\psi}) - \overline{J(\omega, \psi)} \tag{33}$$

and

$$M = \kappa^2 |\overline{S}| \nabla^2 \overline{\omega} - \overline{|S| \nabla^2 \omega} \tag{34}$$

in which $\kappa = \overline{\delta}/\delta$ is the filter width ratio. To avoid division by zero (an inherent possibility in this formulation) [55] proposed the following least-squares adaptation to minimize the error $\langle E^2 \rangle$ given by $E = L - (c_S \delta)^2 M$. We define our averaging operator by

$$\langle f \rangle = \frac{1}{\Omega} \iint f \, dx \, dy \tag{35}$$

where Ω is the area of the basin. The least-squares minimization problem can be solved by differentiating the mean squared error with respect to our model decision variable $(c_S \delta)^2$ to get

$$\frac{\partial \langle E^2 \rangle}{\partial (c_S \delta)^2} = -2 \langle LM \rangle + 2 (c_S \delta)^2 \langle M^2 \rangle. \tag{36}$$

The left hand side of the above equation becomes zero when the error is minimized to give us the following expression for the Smagorinsky constant

$$(c_S \delta)^2 = \frac{|\langle LM \rangle|}{\langle M^2 \rangle}. \tag{37}$$

We also note that the Smagorinsky constant defined by Eq. (37) is always positive definite which is important for the numerical stability in forced-dissipative mesoscale simulations.

A similar derivation may be undertaken for computing the expression for dynamic update using a nonlinear Leith viscosity kernel to obtain

$$(c_L \delta)^3 = \frac{|\langle LM \rangle|}{\langle M^2 \rangle} \tag{38}$$

where

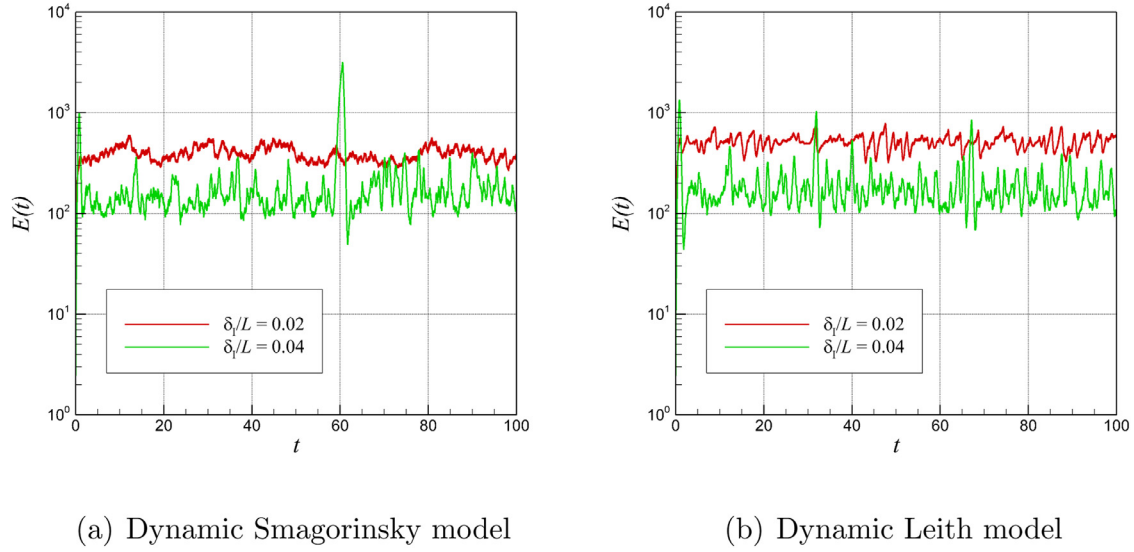$$L = J(\overline{\omega}, \overline{\psi}) - \overline{J(\omega, \psi)} \tag{39}$$

(a) Dynamic Smagorinsky model   (b) Dynamic Leith model

Fig. 3. Time evolution of basin integrated total kinetic energy computed by using a resolution of 256×512.

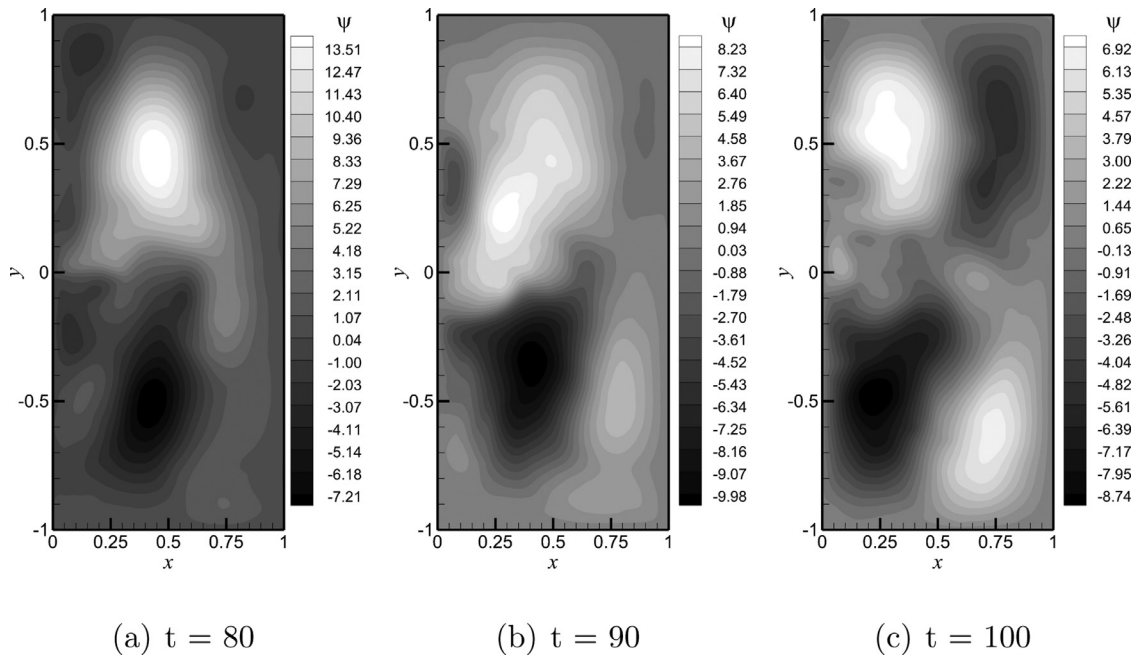(a) t = 80   (b) t = 90   (c) t = 100

Fig. 4. Instantaneous streamfunction plots for Ro = 0.0004 ($\delta_I/L = 0.02$) computed by using the dynamic Smagorinsky model with a resolution of 256×512.

and

$$M = \kappa^3 \overline{|\nabla\omega|\nabla^2\overline{\omega}} - \overline{|\nabla\omega|\nabla^2\omega}. \tag{40}$$

3.4. Low-pass spatial filters

To completely specify the dynamic model given by Eqs. (25) and (37) for the Smagorinsky kernel and by Eqs. (26) and (38) for the Leith kernel, we need to choose a computationally efficient filtering operator. The ability to control the high-frequency content is an essential part of any subgrid-scale

modeling. Therefore various filtering procedures have been suggested and tested for LES computations of turbulent flows (e.g., see [11,67,69,79,94]). Several classes of discrete filters have been tested recently for solving the two-dimensional decaying turbulence problem (e.g., see [80]). It is shown that the following trapezoidal filter yields more accurate results due to its complete attenuation to prevent energy accumulation at the grid cut-off scale. Unless stated otherwise, in this study the filtering ratio κ to the default value of 2. For an arbitrary function f in two dimension, the trapezoidal filter, which is

(a) t = 80   (b) t = 90   (c) t = 100

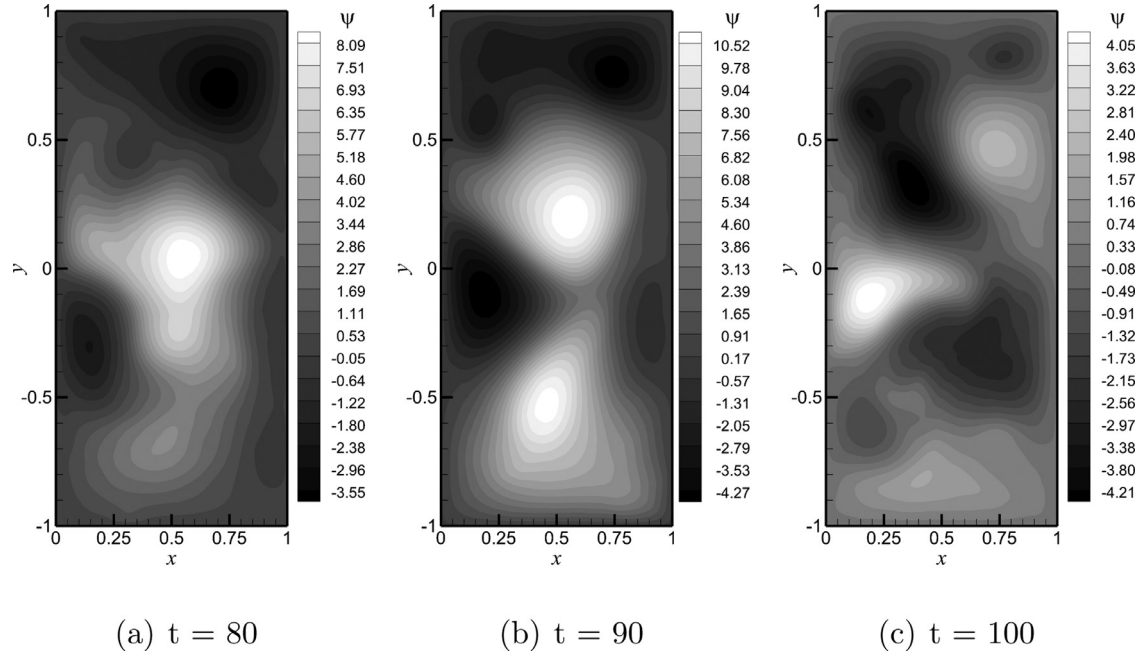Fig. 5. Instantaneous streamfunction plots for Ro = 0.0016 ($\delta_I/L = 0.04$) computed by using the dynamic Smagorinsky model with a resolution of 256×512.
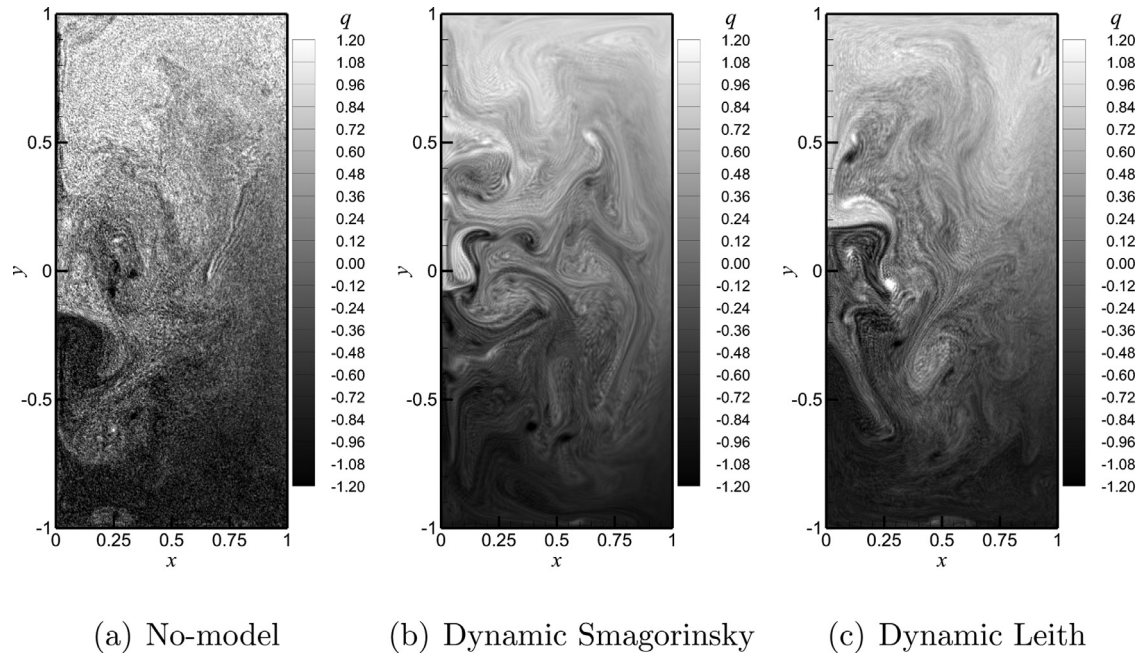

(a) No-model   (b) Dynamic Smagorinsky   (c) Dynamic Leith

Fig. 6. A comparison of subgrid-scale models showing the instantaneous potential vorticity ($q = \mathrm{Ro}\omega + y$) fields at $t = 100$ for Ro = 0.0004 ($\delta_I/L = 0.02$) computed by using a resolution of 256×512.

also known as full-weighting operator, is defined as

$$\bar{f}_{i,j} = \frac{1}{16}(f_{i+1,j+1} + f_{i-1,j+1} + f_{i+1,j-1} + f_{i-1,j-1} \qquad (41)$$

$$+ 2(f_{i+1,j} + f_{i-1,j} + f_{i,j+1} + f_{i,j-1}) + 4f_{i,j})$$

where subscripts i and j refer the discrete grid point indices in the two-dimensional domain. Here, the $\bar{f}$ is the filtered quantity of f coinciding at the boundary nodes. Attenuation characteristics of the filter can be obtained by a modified

wavenumber analysis which leads to the transfer function, $G(k_x, k_y)$, that correlates the Fourier coefficients of the filtered variable to those of the unfiltered variable as follows:

$$\hat{\bar{f}} = G(k_x, k_y)\hat{f} \qquad (42)$$

where $\hat{\bar{f}}$ and $\hat{f}$ are the corresponding Fourier coefficients of the filtered and unfiltered variables, respectively. The transfer
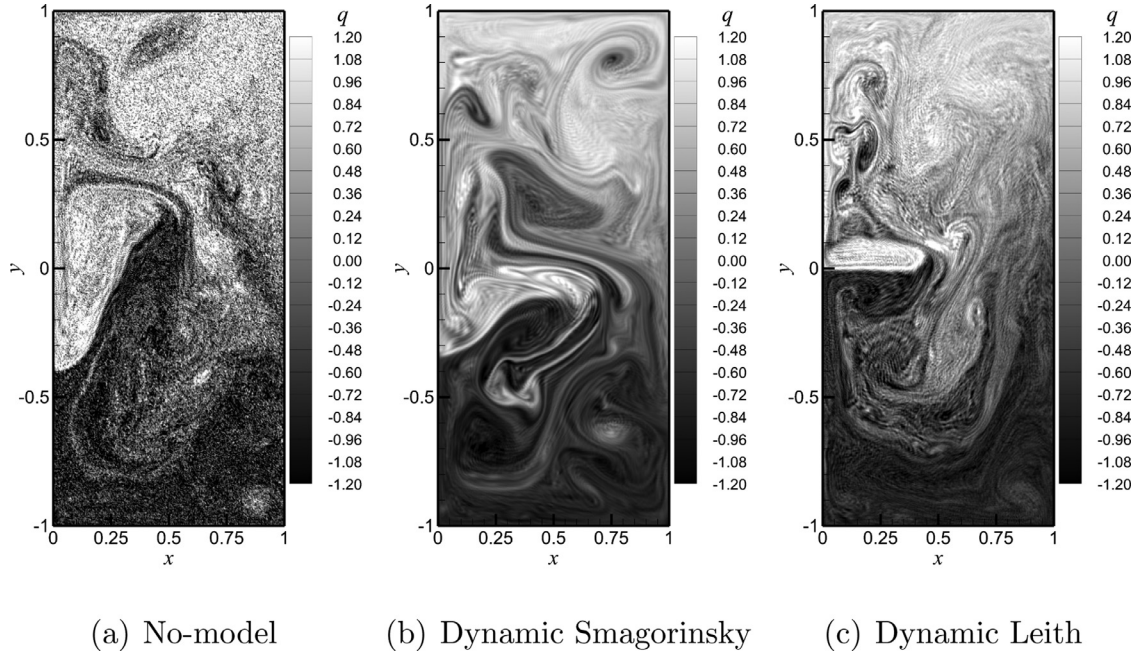
(a) No-model (b) Dynamic Smagorinsky (c) Dynamic Leith

Fig. 7. A comparison of subgrid-scale models showing the instantaneous potential vorticity ($q = \mathrm{Ro}\omega + y$) fields at $t = 100$ for $\mathrm{Ro} = 0.0016$ ($\delta_I/L = 0.04$) computed by using a resolution of 256×512.

function of the trapezoidal filter is

$$G(k_x, k_y) = \frac{1}{4}(1 + \cos(k_x) + \cos(k_y) + \cos(k_x)\cos(k_y)) \quad (43)$$

where k_x and k_y are modified wavenumbers in Fourier space defined between $-\pi$ and $+\pi$. Further details about the filtering procedure can be found in [80]. It should be noted that the trapezoidal filter demonstrates the separability property, an important property for a filter to exhibit due to its performance implications.

4. Numerical methods

4.1. Time integration

In many physically relevant ocean circulation models, such as the QG models, the solutions do not converge to a steady state as time goes to infinity [59]. Rather they remain time dependent by producing a statistically steady state (also known as a quasi-stationary state). Numerical schemes designed for numerical integration of such phenomena should be suited for such behavior of the solutions and for long-time integration. In this section, a brief description of the numerical methods employed in this study is provided using the finite difference framework.

Semi-discrete ordinary differential equations are obtained after a spatial discretization of the partial differential equations [66]. To implement the Runge–Kutta scheme for the time integration (i.e., to be able to use the method of lines), we cast the governing equation given by Eq. (10) in the

following form

$$\frac{d\omega_{i,j}}{dt} = \pounds_{i,j}, \quad (44)$$

where subscripts i and j represent the discrete spatial indices in x- and y-directions, respectively. Here, $\pounds_{i,j}$ denotes the discrete spatial derivative operators, including the convective nonlinear Jacobian, β-plane approximation of the Coriolis force, the linear Laplacian diffusive term, and the double-gyre wind forcing stress term (e.g., see Eq. (46)). We assume that the numerical approximation for time level n is known, and we seek the numerical approximation for time level $n + 1$, after the time step Δt. The optimal third-order accurate total variation diminishing Runge–Kutta (TVDRK3) scheme is then given as [33]

$$\omega_{i,j}^{(1)} = \omega_{i,j}^{(n)} + \Delta t \pounds_{i,j}^{(n)},$$
$$\omega_{i,j}^{(2)} = \frac{3}{4}\omega_{i,j}^{(n)} + \frac{1}{4}\omega_{i,j}^{(1)} + \frac{1}{4}\Delta t \pounds_{i,j}^{(1)},$$
$$\omega_{i,j}^{(n+1)} = \frac{1}{3}\omega_{i,j}^{(n)} + \frac{2}{3}\omega_{i,j}^{(2)} + \frac{2}{3}\Delta t \pounds_{i,j}^{(2)} \quad (45)$$

where Δt is the adaptive time step, which can be computed at the end of each time step by specifying the Courant–Friedrichs–Lewy (CFL) number satisfying the numerical stability criterion, which is given by CFL ≤ 1 for the TVDRK3 scheme. The CFL number is set to 0.9 in the present study to ensure numerical stability. The TVDRK3 scheme has been extensively used to compute hyperbolic conservation laws (e.g., see [34] and references therein). It has been also shown that the TVDRK3 predicts slightly more accurate results than some other third-order Runge–Kutta schemes for solving two-dimensional incompressible flow problems [81].
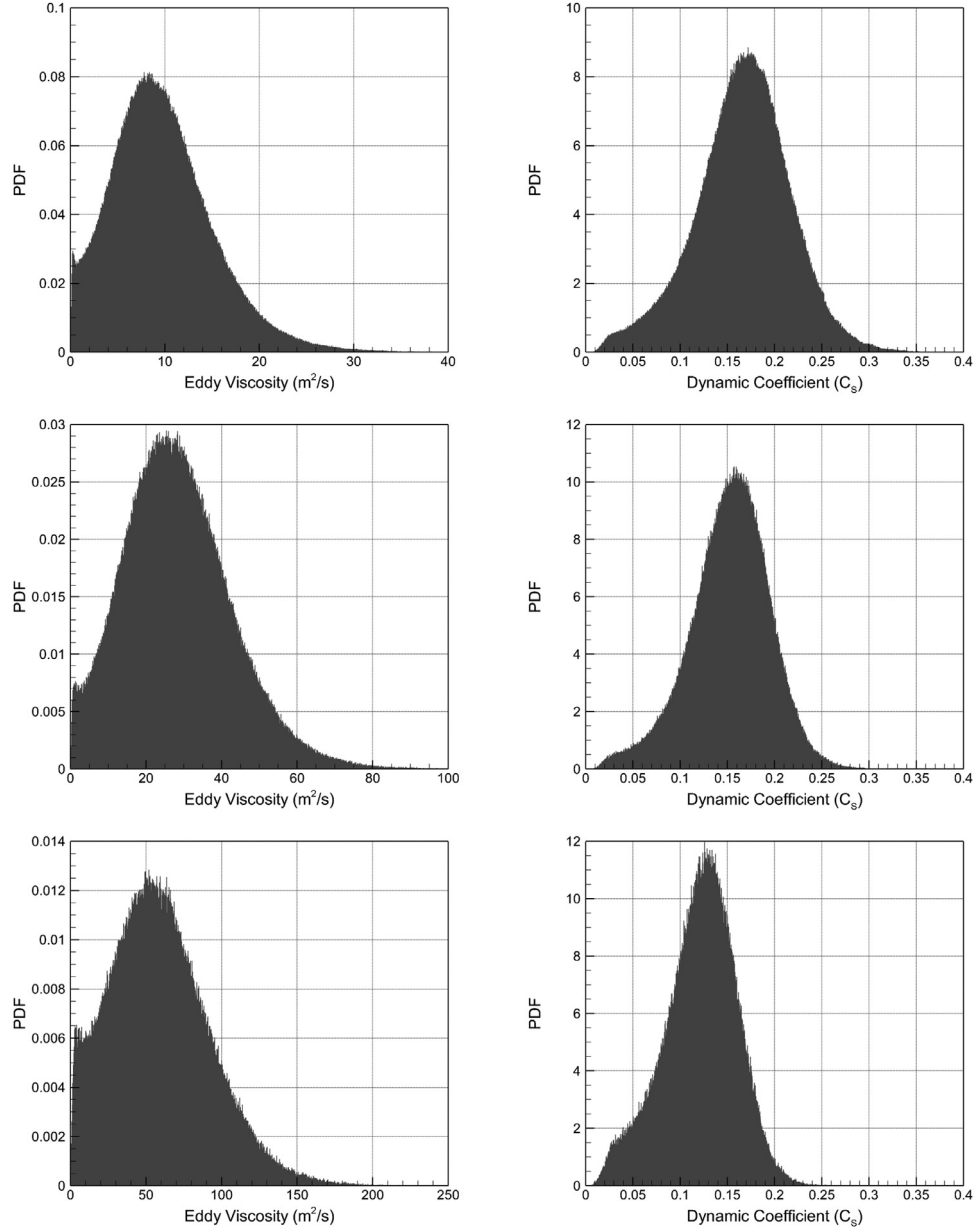
Fig. 8. One-layer numerical experiments for Ro = 0.0004 with the dynamic Smagorinsky model: normalized probability density function (PDF) distributions for the eddy viscosity coefficient and the Smagorinsky constant dynamically modeled by the proposed method using resolutions of 256×512 (top row), 128×256 (middle row), and 64×128 (bottom row).

4.2. Numerical discretizations

The source term of a particular layer, $\pounds_{i,j}$, is written as

$$\pounds_{i,j} = -J(\omega_{i,j}, \psi_{i,j}) + \frac{1}{\text{Ro}} \frac{\partial \psi_{i,j}}{\partial x} + A\nabla^2\omega_{i,j} + \frac{1}{\text{Ro}} \sin(\pi y) \tag{46}$$

where we use the standard second-order central finite difference schemes in linear terms. Therefore, the derivative operators in Eq. (46) can be written in discrete form as:

$$\frac{\partial \psi_{i,j}}{\partial x} = \frac{\psi_{i+1,j} - \psi_{i-1,j}}{2\Delta x}, \tag{47}$$

$$\nabla^2\omega_{i,j} = \frac{\omega_{i+1,j} - 2\omega_{i,j} + \omega_{i-1,j}}{\Delta x^2} + \frac{\omega_{i,j+1} - 2\omega_{i,j} + \omega_{i,j-1}}{\Delta y^2} \tag{48}$$

where Δx and Δy are the mesh sizes in x- and y-directions, respectively.

For the modeling of the nonlinear term, Arakawa [2] suggested that the conservation of energy, enstrophy, and skew-symmetry is sufficient to avoid computational instabilities stemming from nonlinear interactions. The following second-order Arakawa scheme for the Jacobian is written as

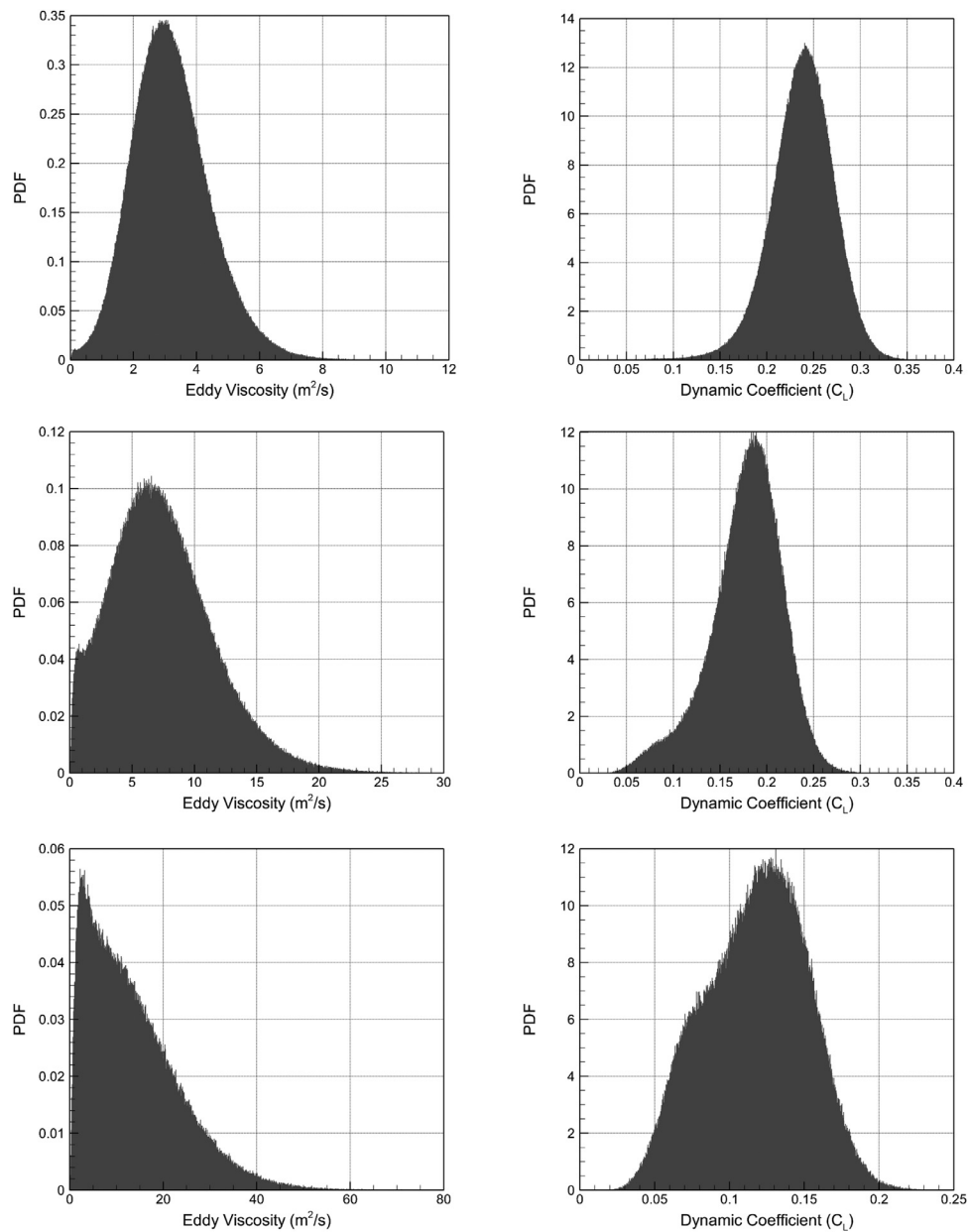$$J(\omega_{i,j}, \psi_{i,j}) = \frac{1}{3}(J_1 + J_2 + J_3) \tag{49}$$

Fig. 9. One-layer numerical experiments for Ro = 0.0004 with the dynamic Leith model: normalized probability density function (PDF) distributions for the eddy viscosity coefficient and the Leith constant dynamically modeled by the proposed method using resolutions of 256×512 (top row), 128×256 (middle row), and 64×128 (bottom row).

Table 2
Dynamic Smagorinsky modeling of the one-layer experiment for Ro=0.0004 ($\delta_I/L = 0.02$): mean values of the eddy viscosity coefficient and the Smagorinsky constant (considering both space and time averaging).

Filter ratio	256×512		128×256		64×128	
	ν_e (m²/s)	c_S	ν_e (m²/s)	c_S	ν_e (m²/s)	c_S
$\kappa = 2$	9.78	0.16	28.42	0.15	59.07	0.12
$\kappa = \sqrt{6}$	3.02	0.084	10.05	0.078	24.63	0.062
$\kappa = 3$	1.14	0.048	3.66	0.043	10.06	0.035

Table 3
Dynamic Smagorinsky modeling of the one-layer experiment for Ro=0.0016 ($\delta_I/L = 0.04$): mean values of the eddy viscosity coefficient and the Smagorinsky constant (considering both space and time averaging).

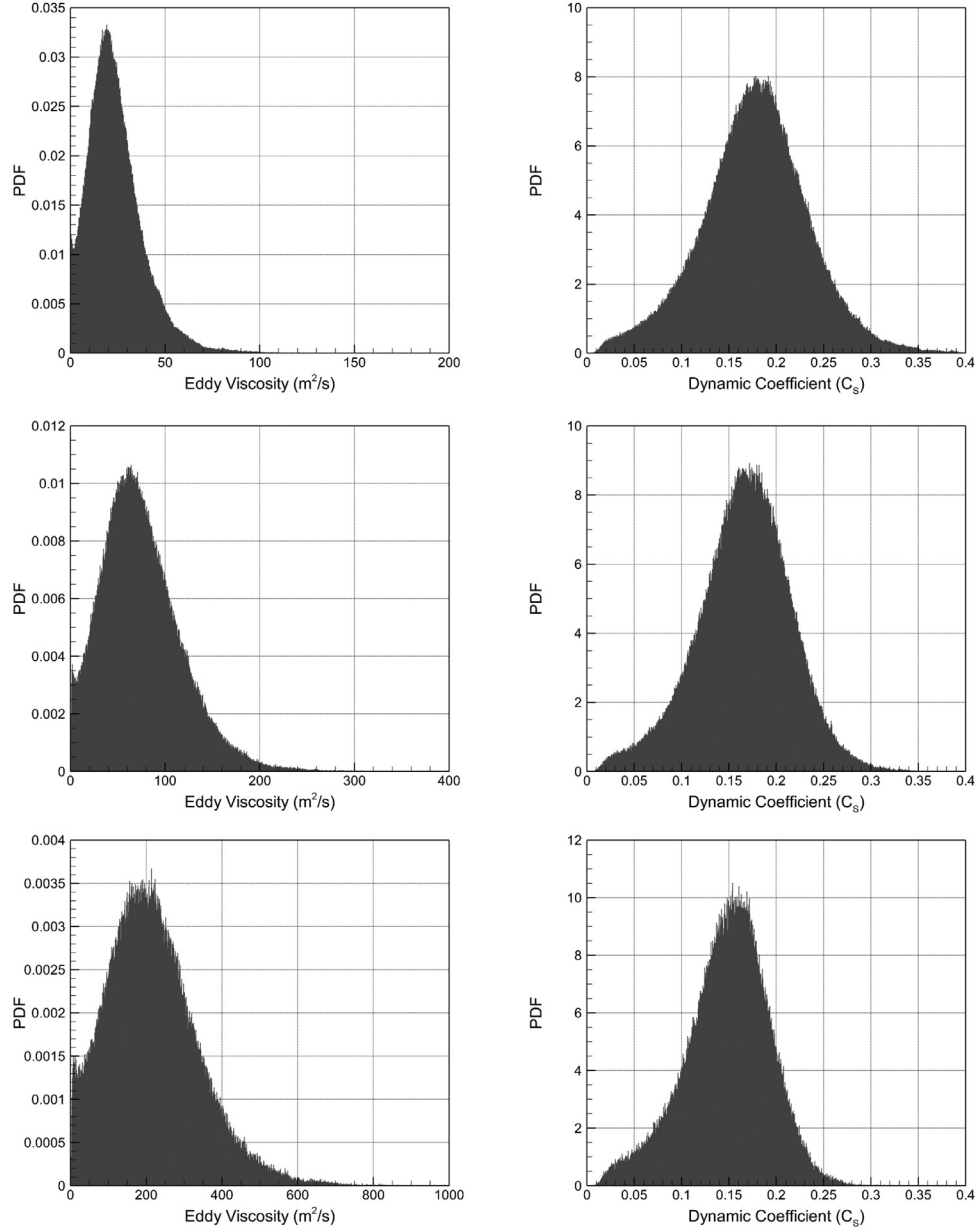| Filter ratio	256×512		128×256		64×128	
	ν_e (m²/s)	c_S	ν_e (m²/s)	c_S	ν_e (m²/s)	c_S
$\kappa = 2$	24.74	0.18	75.31	0.17	218.22	0.15
$\kappa = \sqrt{6}$	6.94	0.091	25.07	0.089	75.71	0.078
$\kappa = 3$	2.42	0.051	6.80	0.049	27.64	0.043

Fig. 10. One-layer numerical experiments for Ro = 0.0016 with the dynamic Smagorinsky model: normalized probability density function (PDF) distributions for the eddy viscosity coefficient and the Smagorinsky constant dynamically modeled by the proposed method using resolutions of 256×512 (top row), 128×256 (middle row), and 64×128 (bottom row).

where the discrete Jacobians have the following forms:

$$
J_1 = \frac{1}{4\Delta x \Delta y} \Big[(\omega_{i+1,j} - \omega_{i-1,j})(\psi_{i,j+1} - \psi_{i,j-1})
$$
$$
- (\omega_{i,j+1} - \omega_{i,j-1})(\psi_{i+1,j} - \psi_{i-1,j}) \Big], \tag{50}
$$

$$
J_2 = \frac{1}{4\Delta x \Delta y} [\omega_{i+1,j}(\psi_{i+1,j+1} - \psi_{i+1,j-1}) - \omega_{i-1,j}(\psi_{i-1,j+1}
$$
$$
- \psi_{i-1,j-1}) - \omega_{i,j+1}(\psi_{i+1,j+1} - \psi_{i-1,j+1})
$$
$$
+ \omega_{i,j-1}(\psi_{i+1,j-1} - \psi_{i-1,j-1})], \tag{51}
$$

$$
J_3 = \frac{1}{4\Delta x \Delta y} [\omega_{i+1,j+1}(\psi_{i,j+1} - \psi_{i+1,j})
$$
$$
- \omega_{i-1,j-1}(\psi_{i-1,j} - \psi_{i,j-1})
$$
$$
- \omega_{i-1,j+1}(\psi_{i,j+1} - \psi_{i-1,j}) + \omega_{i+1,j-1}(\psi_{i+1,j} - \psi_{i,j-1})]. \tag{52}
$$

Note that J_1, which corresponds to the central second-order difference scheme, is not sufficient for the conservation of energy, enstrophy, and skew-symmetry by the numerical discretization. Arakawa [2] showed that the judicious combination of J_1, J_2, and J_3 in Eq. (49) achieves the above discrete conservation properties.
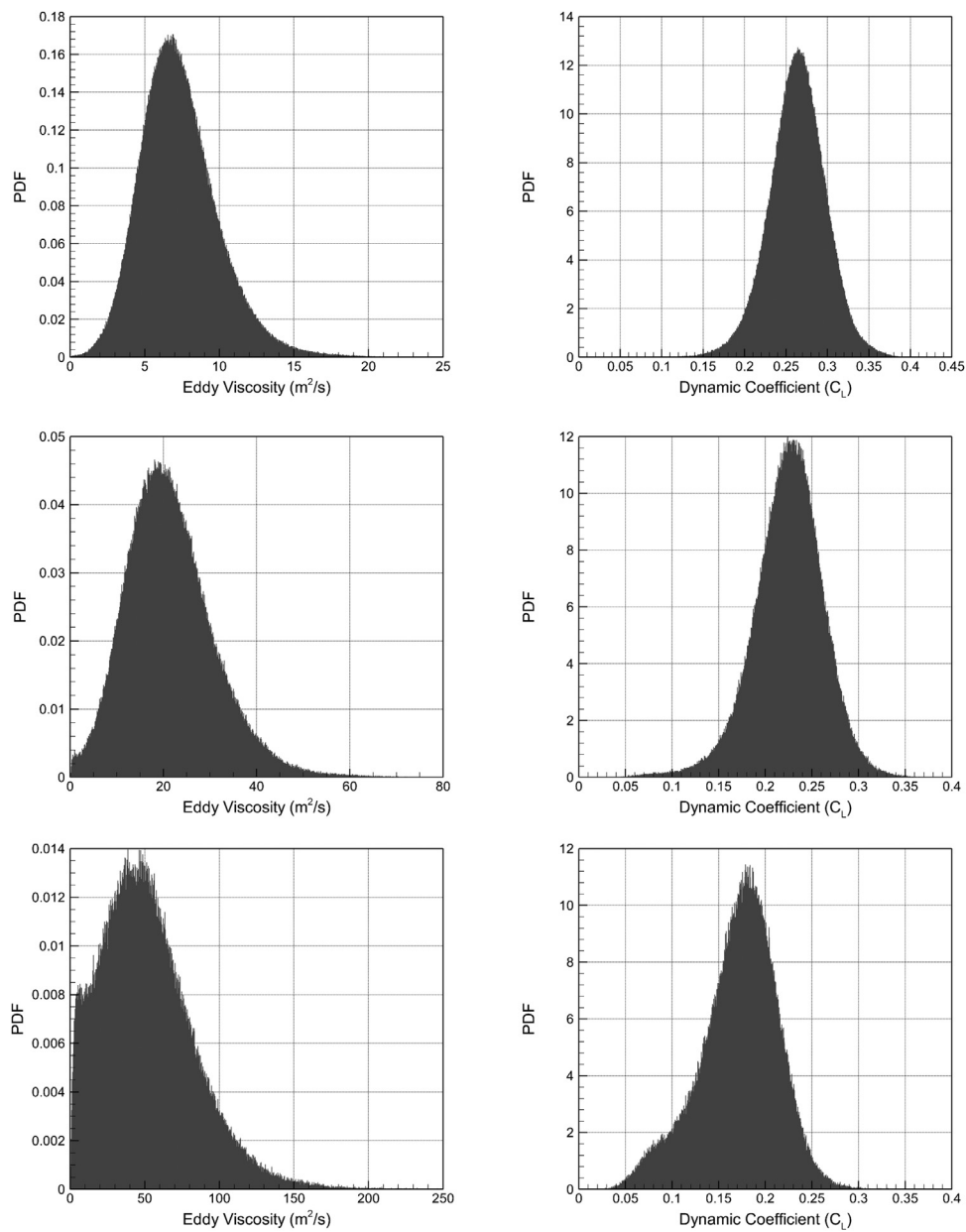
Fig. 11. One-layer numerical experiments for Ro = 0.0016 with the dynamic Leith model: normalized probability density function (PDF) distributions for the eddy viscosity coefficient and the Leith constant dynamically modeled by the proposed method using resolutions of 256×512 (top row), 128×256 (middle row), and 64×128 (bottom row).

Table 4
Dynamic Leith modeling of the one-layer experiment for Ro=0.0004 ($\delta_I/L = 0.02$): mean values of the eddy viscosity coefficient and the Leith constant (considering both space and time averaging).

Filter ratio	256×512		128×256		64×128	
	ν_e (m^2/s)	c_L	ν_e (m^2/s)	c_L	ν_e (m^2/s)	c_L
$\kappa = 2$	3.20	0.24	7.43	0.18	13.58	0.12
$\kappa = \sqrt{6}$	1.01	0.14	2.19	0.1	4.50	0.069
$\kappa = 3$	0.36	0.087	0.82	0.064	1.71	0.045

Table 5
Dynamic Leith modeling of the one-layer experiment for Ro=0.0016 ($\delta_I/L = 0.04$): mean values of the eddy viscosity coefficient and the Leith constant (considering both space and time averaging).

Filter ratio	256×512		128×256		64×128	
	ν_e (m^2/s)	c_L	ν_e (m^2/s)	c_L	ν_e (m^2/s)	c_L
$\kappa = 2$	7.34	0.26	21.50	0.23	52.07	0.17
$\kappa = \sqrt{6}$	2.14	0.15	5.48	0.12	12.67	0.088
$\kappa = 3$	0.71	0.094	1.66	0.07	3.98	0.053

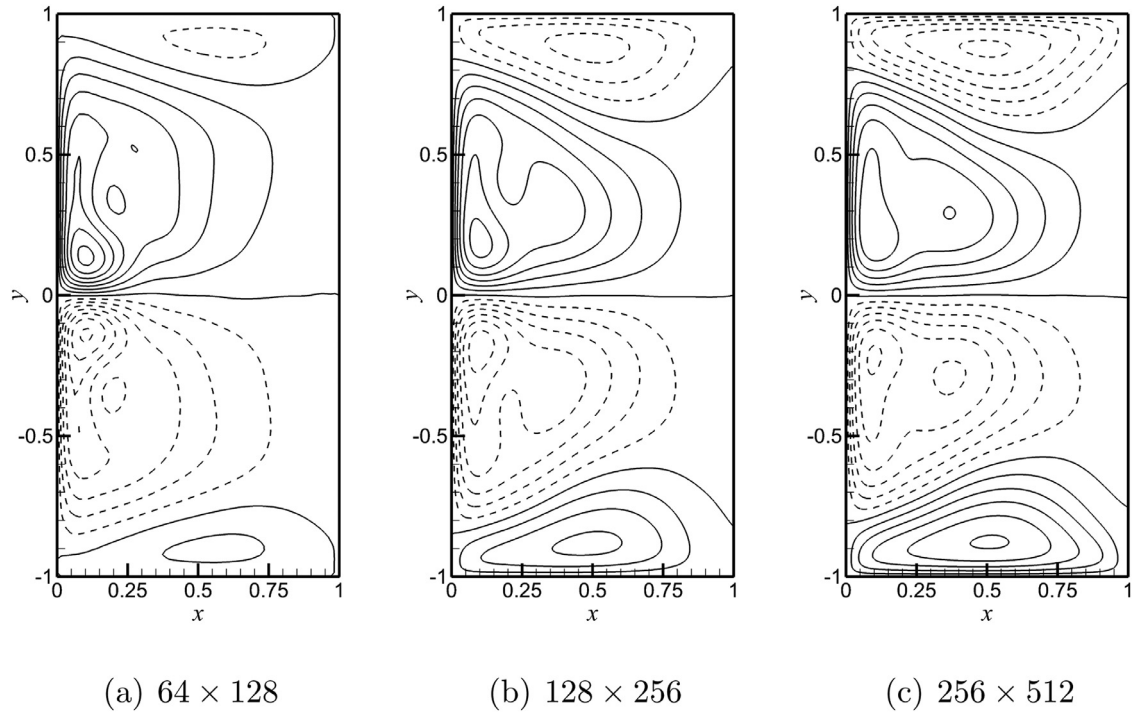(a) 64×128 (b) 128×256 (c) 256×512

Fig. 12. Mean streamfunction contour plots computed by using the dynamic Smagorinsky model on various resolutions for the case of Ro = 0.0004 ($\delta_I/L = 0.02$). An equidistant contour interval of $\Delta\psi = 0.2$ is used.

4.3. Inversion subproblem for one-layer model

Most of the demand on computing resources posed by QG models comes in the solution of the elliptic Poisson equation [62]. This is also true for our study to find streamfunction val-ues from updated vorticity values at each substep in the time integration. However, taking advantage of the simple Carte-sian domain and uniform grid spacing, an efficient fast Fourier transform (FFT) method is utilized for solving the kinematic relationship given in Eq. (3). Specifically, the discrete form
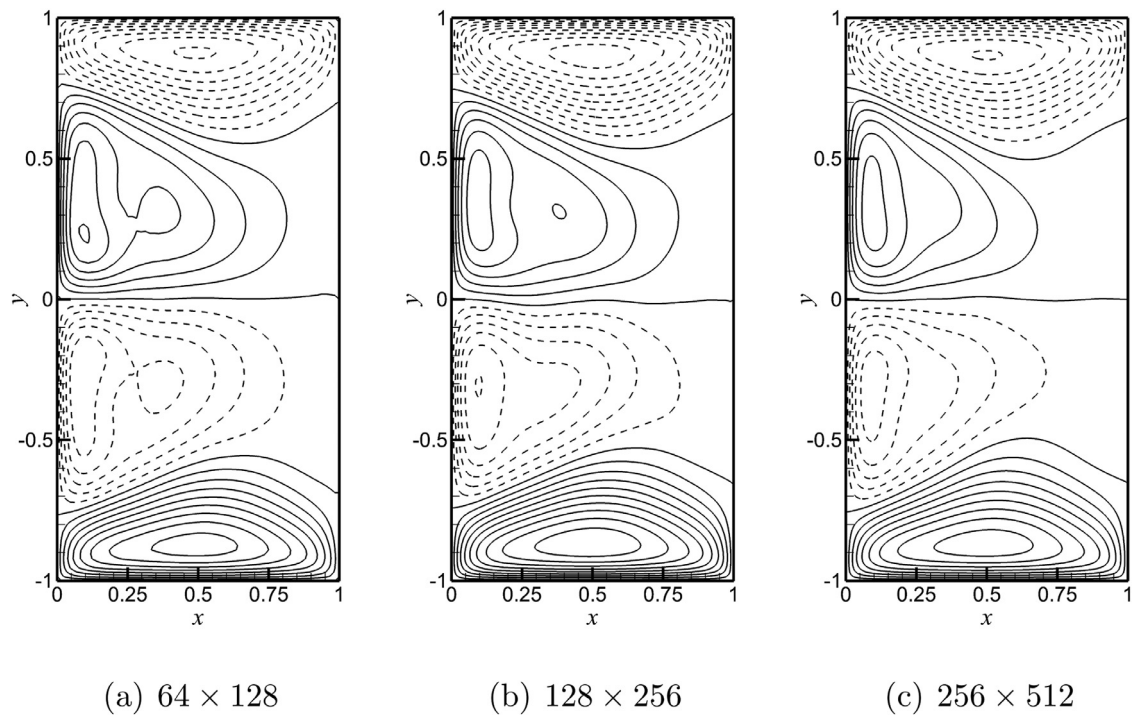

(a) 64×128 (b) 128×256 (c) 256×512

Fig. 13. Mean streamfunction contour plots computed by using the dynamic Leith model on various resolutions for the case of Ro = 0.0004 ($\delta_I/L = 0.02$). An equidistant contour interval of $\Delta\psi = 0.2$ is used.

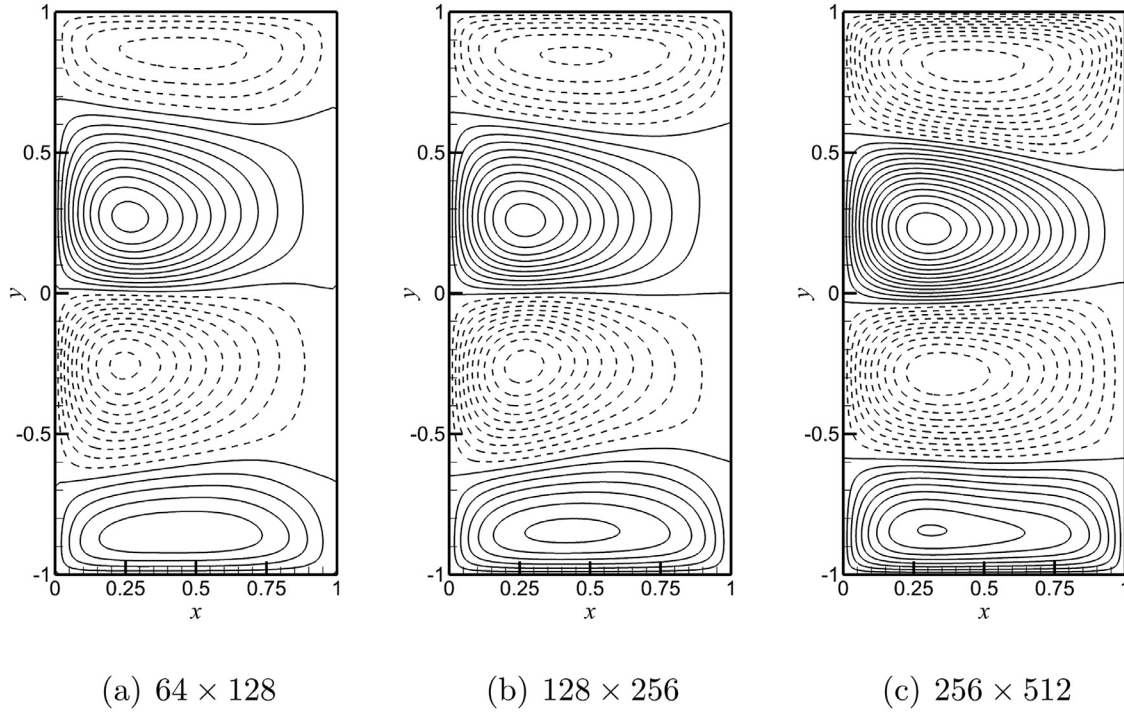(a) 64×128 (b) 128×256 (c) 256×512

Fig. 14. Mean streamfunction contour plots computed by using the dynamic Smagorinsky model on various resolutions for the case of Ro = 0.0016 ($\delta_I/L = 0.04$). An equidistant contour interval of $\Delta\psi = 0.2$ is used.

of Eq. (3) is given by

$$\frac{\psi_{i+1,j} - 2\psi_{i,j} + \psi_{i-1,j}}{\Delta x^2} + \frac{\psi_{i,j+1} - 2\psi_{i,j} + \psi_{i,j-1}}{\Delta y^2} = -\omega_{i,j},$$

(53)

and our boundary conditions suggest the use of a fast sine transform. The procedure to solve Eq. (53) involves three steps. First, an inverse sine transform for the source term
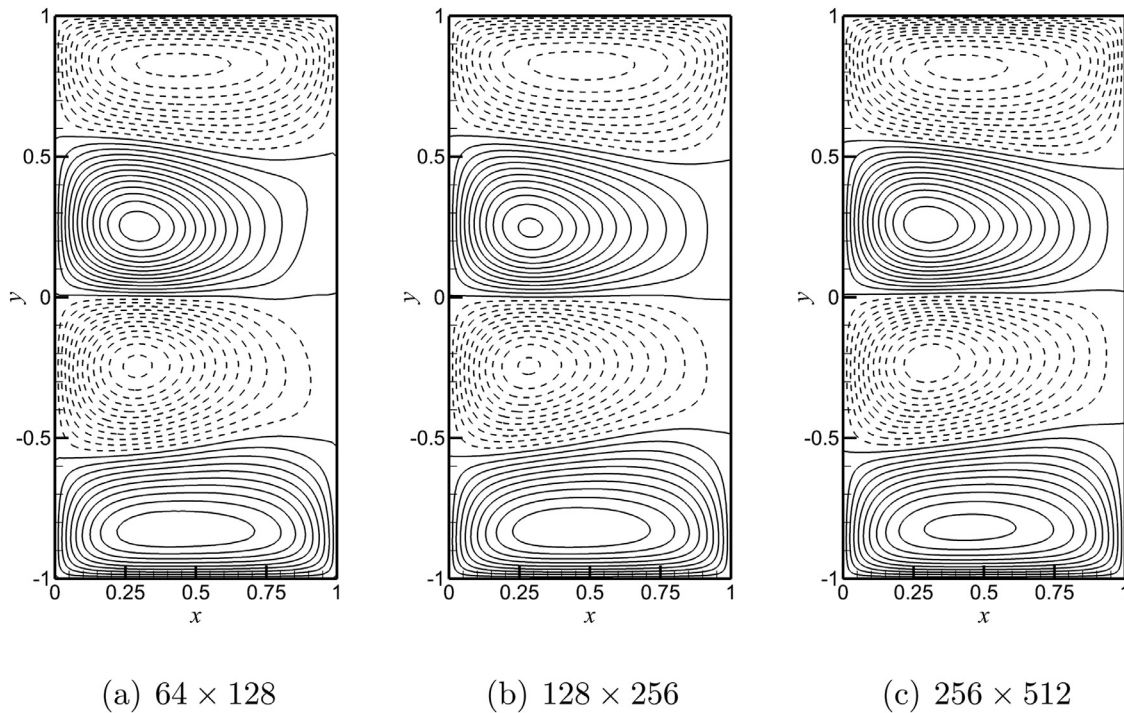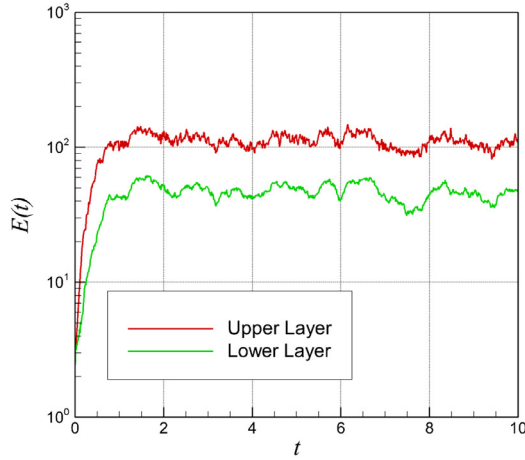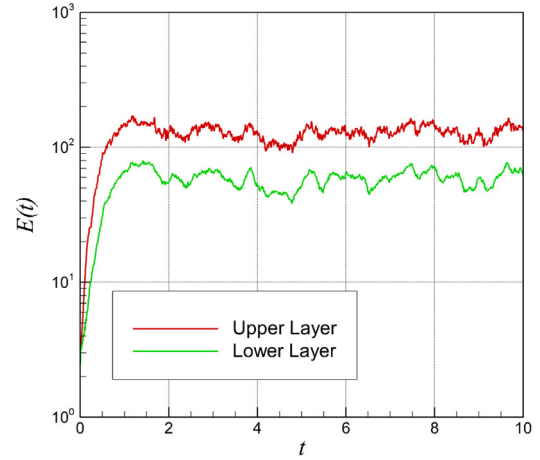

(a) 64×128 (b) 128×256 (c) 256×512

Fig. 15. Mean streamfunction contour plots computed by using the dynamic Leith model on various resolutions for the case of Ro = 0.0016 ($\delta_I/L = 0.04$). An equidistant contour interval of $\Delta\psi = 0.2$ is used.

(a) Dynamic Smagorinsky model   (b) Dynamic Leith model

Fig. 16. Time evolution of basin integrated total kinetic energy computed by using a resolution of 512×512.

is given by:

$$\hat{\omega}_{k,l} = \frac{2}{N} \frac{2}{M} \sum_{i=1}^{N-1} \sum_{j=1}^{M-1} \omega_{i,j} \sin\left(\frac{\pi k i}{N}\right) \sin\left(\frac{\pi l j}{M}\right), \tag{54}$$

where N and M are the total number of grid points in x and y directions. Here the symbol hat is used to represent the corresponding Fourier coefficient of the physical grid data with a subscript pair i, j, where $i = 0, 1, \ldots N$ and $j = 0, 1, \ldots M$. As a second step, we directly solve Eq. (53) in Fourier space:

$$\hat{\psi}_{k,l} = -\frac{\hat{\omega}_{k,l}}{\frac{2}{\Delta x^2}\left(\cos\left(\frac{\pi k}{N}\right) - 1\right) + \frac{2}{\Delta y^2}\left(\cos\left(\frac{\pi l}{M}\right) - 1\right)}. \tag{55}$$

Finally, the streamfunction values are found by performing a forward sine transform:

$$\psi_{i,j} = \sum_{k=1}^{N-1} \sum_{l=1}^{M-1} \hat{\psi}_{k,l} \sin\left(\frac{\pi k i}{N}\right) \sin\left(\frac{\pi l j}{M}\right). \tag{56}$$

The computational cost of this elliptic solver is $\mathcal{O}(NM \log(N) \log(M))$. The FFT algorithm given by Press et al. [76] is used for forward and inverse sine transforms.

4.4. Inversion subproblem for two-layer model

The QG2 inversion subproblem given by Eq. (20) may also be solved by a FFT based direct inversion. As mentioned in the previous sections, fast Sine transforms are used for each layer due to the impermeability boundary conditions given by

$$\hat{\omega}_{1_{k,l}} = \frac{2}{N} \frac{2}{M} \sum_{i=1}^{N-1} \sum_{j=1}^{M-1} \omega_{1_{i,j}} \sin\left(\frac{\pi k i}{N}\right) \sin\left(\frac{\pi l j}{M}\right) \tag{57}$$

$$\hat{\omega}_{2_{k,l}} = \frac{2}{N} \frac{2}{M} \sum_{i=1}^{N-1} \sum_{j=1}^{M-1} \omega_{2_{i,j}} \sin\left(\frac{\pi k i}{N}\right) \sin\left(\frac{\pi l j}{M}\right) \tag{58}$$

where N and M have been defined previously. We can now solve the subproblem directly in Fourier space through

$$\hat{\psi}_1 = \frac{(-\alpha + c)\hat{\omega}_1 + b\hat{\omega}_2}{\alpha(\alpha - b - c)} \tag{59}$$

$$\hat{\psi}_2 = \frac{c\hat{\omega}_1 + (-\alpha + b)\hat{\omega}_2}{\alpha(\alpha - b - c)} \tag{60}$$

where

$$\alpha = \frac{2}{\Delta x^2}\left[\cos\left(\frac{\pi k}{N}\right) - 1\right] + \frac{2}{\Delta y^2}\left[\cos\left(\frac{\pi l}{M}\right) - 1\right] \tag{61}$$

and

$$b = \frac{\text{Fr}}{\delta \, \text{Ro}} \qquad c = \frac{\text{Fr}}{(1 - \delta)\text{Ro}}. \tag{62}$$

We are left with the task to perform the forward sine transform using

$$\psi_{1_{i,j}} = \sum_{k=1}^{N-1} \sum_{l=1}^{M-1} \hat{\psi}_{1_{k,l}} \sin\left(\frac{\pi k i}{N}\right) \sin\left(\frac{\pi l j}{M}\right) \tag{63}$$

$$\psi_{2_{i,j}} = \sum_{k=1}^{N-1} \sum_{l=1}^{M-1} \hat{\psi}_{2_{k,l}} \sin\left(\frac{\pi k i}{N}\right) \sin\left(\frac{\pi l j}{M}\right). \tag{64}$$

The FFT algorithm used and its computational cost of this subproblem is identical to the one-layer QG problem.

5. Results and discussion

5.1. One-layer QG1 experiments

In this section, the dynamic subgrid-scale eddy viscosity model proposed in Section 3 will be tested using the one-layer quasigeostrophic (QG) ocean model given by Section 2. The
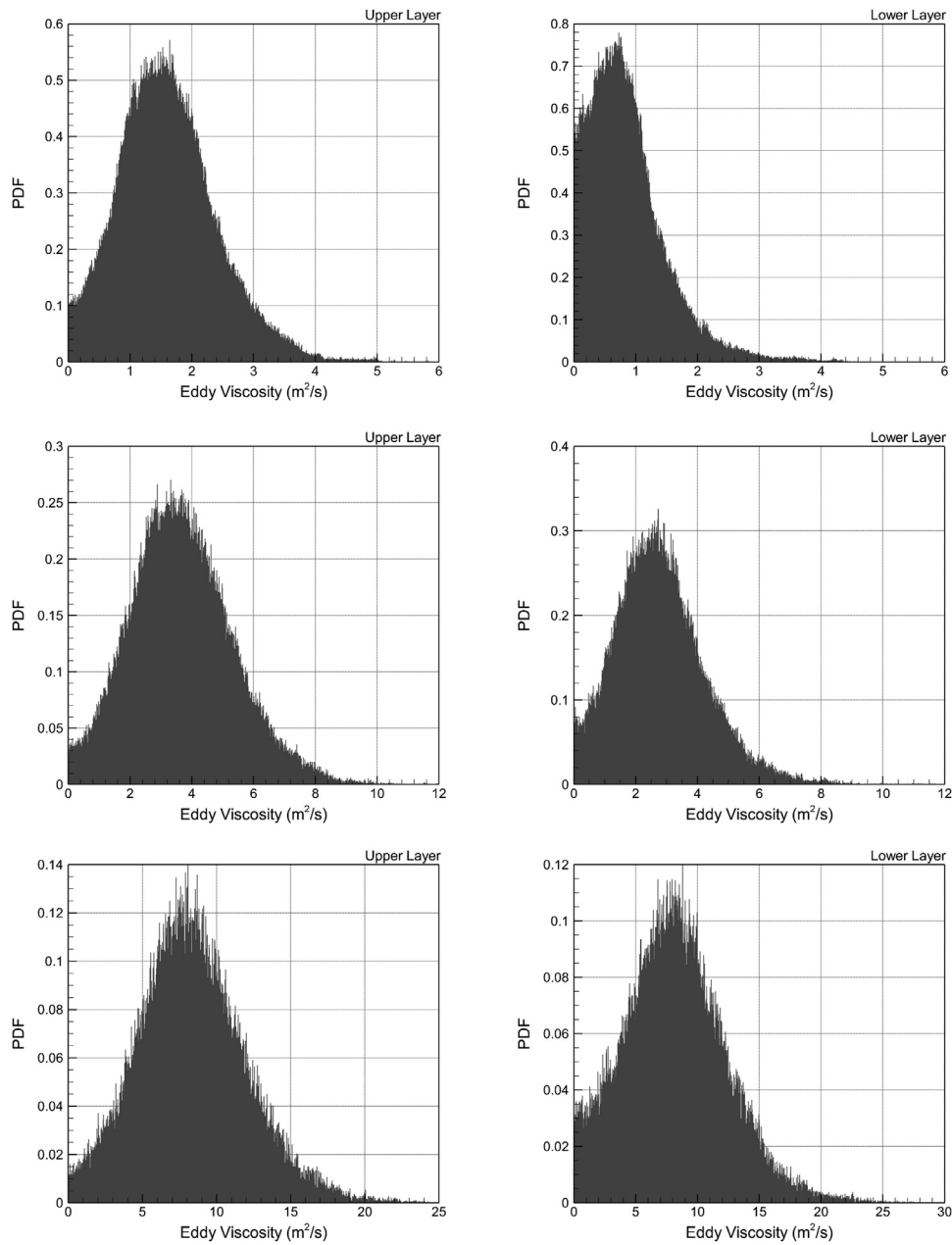
Fig. 17. Normalized probability density function (PDF) distributions of the eddy viscosity coefficient for the two-layer numerical experiments using the dynamic Smagorinsky model with resolutions of 512×512 (top row), 256×256 (middle row), and 128×128 (bottom row).

approach is applied to the four-gyre mid-latitude ocean circulation problem. The model is applied to a beta-plane simplified ocean basin defined in $x \in [0, 1]$ and $y \in [-1, +1]$ using dimensionless Cartesian coordinates, which is a standard prototype of more realistic ocean dynamics. This test problem has been used in numerous studies (e.g., [16,35,42,68,84]) and represents an ideal setting for the numerical assessment of the subgrid-scale parametrization. The QG model driven by a symmetric double-gyre wind forcing should yield a four-gyre circulation pattern in the time mean. We will investigate numerically whether the proposed dynamic model can reproduce the four-gyre pattern for varying the computational

resolution. In most of the ocean circulation simulations, the amount of eddy viscosity is determined by using the definition of Munk scale, $\delta_M = (\nu_e/\beta)^{1/3}$, for the viscous boundary layer in such a way that the computational grid scale should be smaller than the Munk scale (e.g., see [82] for further discussion). In the first approximation, this approach provides an excessive dissipation in most parts of the ocean basin. Using an inverse approach, however, in this study we will focus on assessing the eddy viscosity coefficient dynamically computed in each numerical experiment and address the intimate relationship between the eddy viscosities and the numerical resolution employed by the QG models.
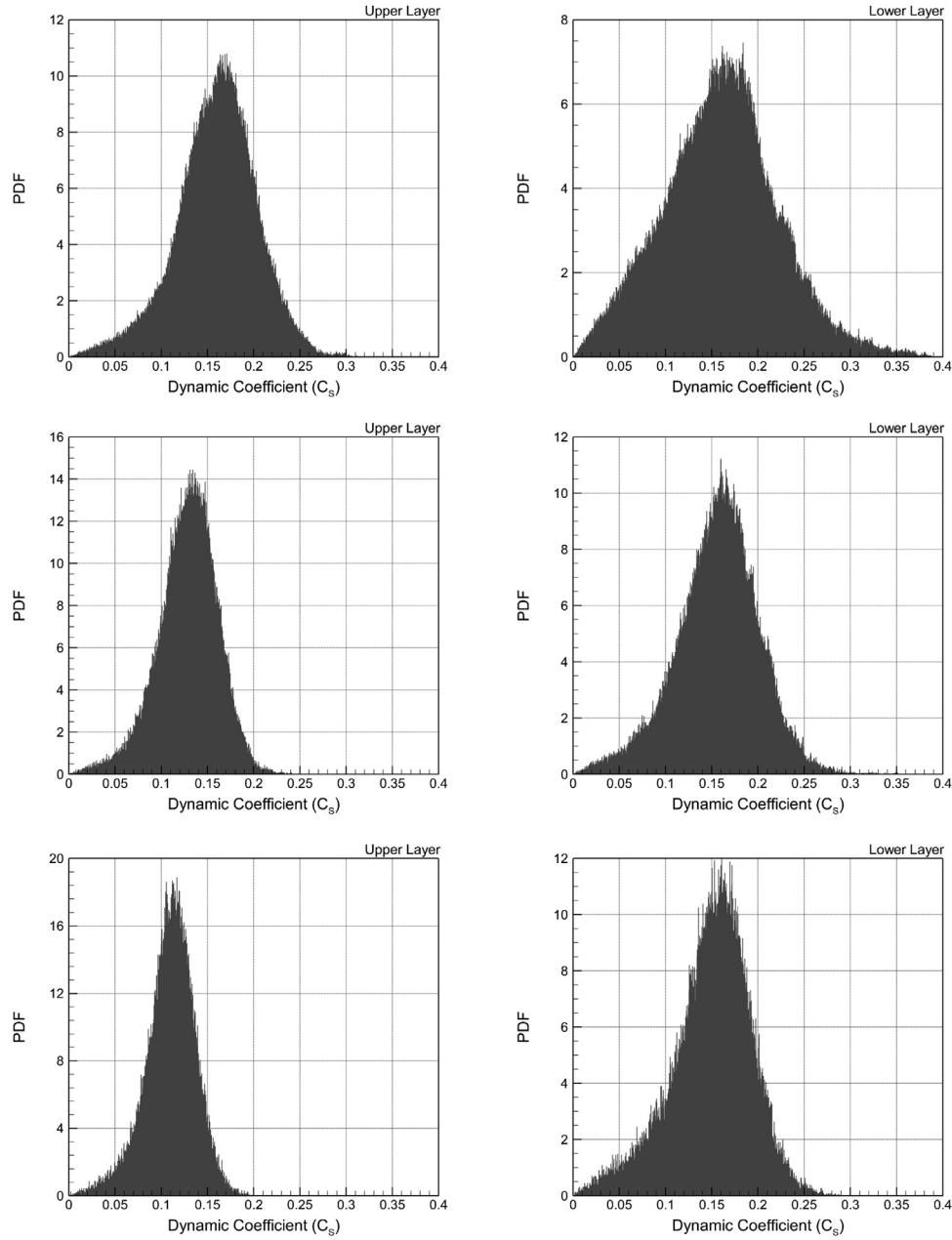
Fig. 18. Normalized probability density function (PDF) distributions of the dynamic coefficient for the two-layer numerical experiments using the dynamic Smagorinsky model with resolutions of 512×512 (top row), 256×256 (middle row), and 128×128 (bottom row).

Starting from a quiescent state, all numerical experiments conducted in this section are solved for a maximum dimensionless time of $t_{max} = 100$, which is long enough to capture statistically steady states after an initial transient period. Here, we use three consecutive resolutions for two different physical settings varying with the Rhines scale, namely performing experiments for $\delta_I/L = 0.02$ (Ro=0.0004), and $\delta_I/L = 0.04$ (Ro=0.0016). The dimensionless eddy viscosity coefficient A is computed dynamically using the proposed models (i.e., using Smagorinsky's and Leith's viscosity kernels) presented in Section 3. Although we solve the dimensionless form of the governing equations, we use standard values of $\beta = 1.75 \times 10^{-11}$ m^{-1} s^{-1} and $L = 2000$ km when

presenting the dimensional form of the eddy viscosity data (i.e., the relationship between dimensional and dimensionless quantities is given by Eq. (11)).

In Fig. 3, we plot the time evolution of the basin integrated total kinetic energy given by,

$$E(t) = \frac{1}{2}\frac{1}{\Omega} \iint_{\Omega} \left(\left(\frac{\partial \psi}{\partial x}\right)^2 + \left(\frac{\partial \psi}{\partial y}\right)^2\right) dxdy \qquad (65)$$

for each numerical experiment using a resolution of 256×512 between $t = 0$ and $t = 100$ comparing the Smagorinsky and Leith viscosity kernels. The dimensionless time unit corresponds to approximately 2.25 and 0.55 years for the numerical experiments performed at Ro = 0.0004 and 0.0016, re-
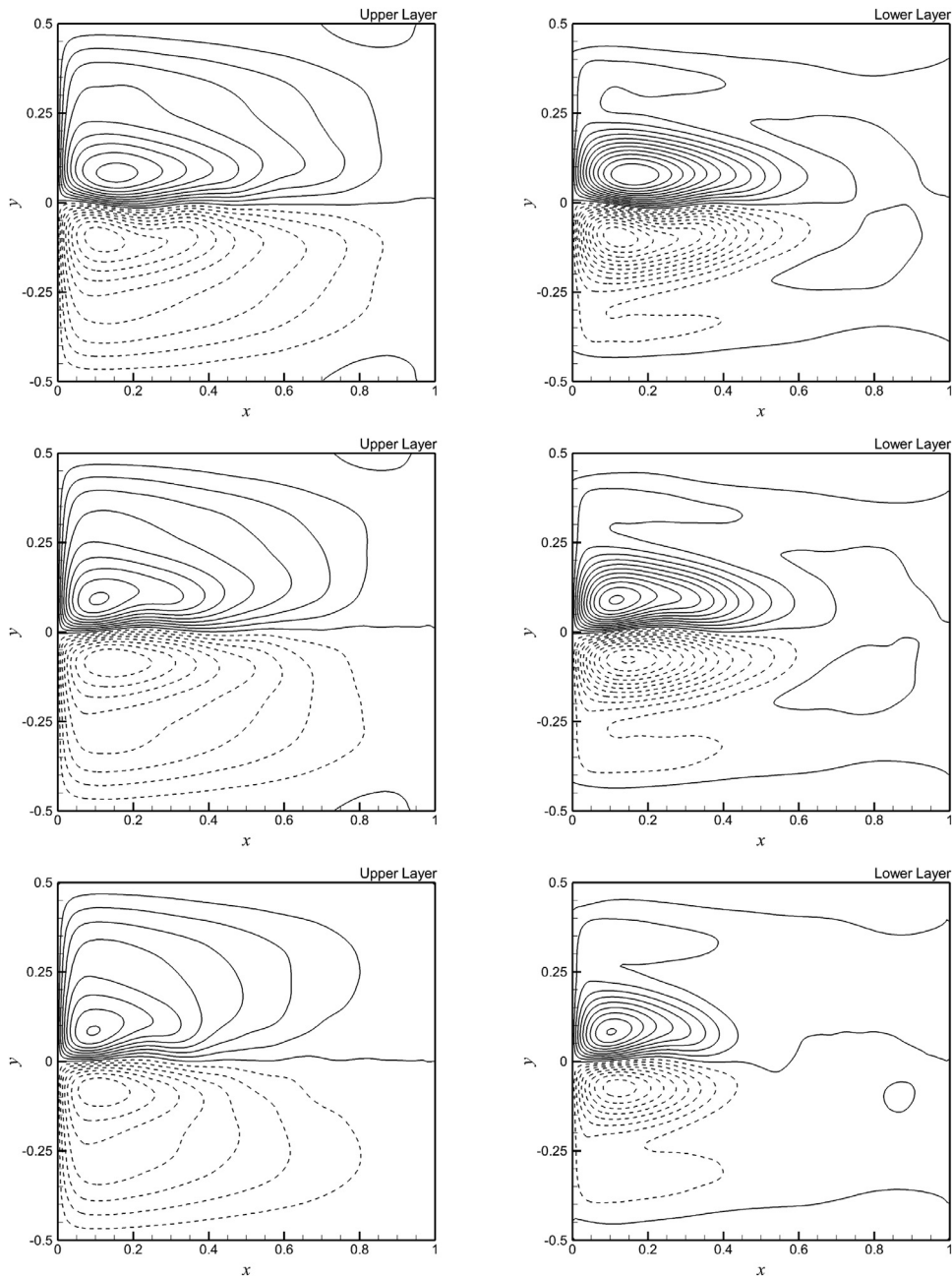
Fig. 19. Mean streamfunction contour plots for the two-layer numerical experiments using the dynamic Smagorinsky model with resolutions of 512×512 (top row), 256×256 (middle row), and 128×128 (bottom row). An equidistant contour interval of $\Delta \psi = 0.1$ is used.

spectively (i.e., the reference scale reads as $L/V = (Ro \beta L)^{-1}$ for the time nondimensionalization). As shown in this figure, after an initial transition period, a quasi-stationary regime is achieved in each experiment showing both inter-annual and inter-decadal variability of the ocean dynamics. Representative instantaneous flow fields are shown in Fig. 4 for Ro $= 0.0004$ illustrating the dimensionless streamfunction contours at $t = 80$, $t = 90$, and $t = 100$. Similar instantaneous streamfunction contours are also plotted in Fig. 5 for Ro $= 0.0016$. Although instantaneous flow dynamics in the basin shows chaotic behaviur, the mean four-gyre circulation patterns emerge when we average over years. These patterns

are simply the nature of beta and wind stress curl effects rather than the effect of the subgrid-scale physics. As shown in Figs. 6 and 7, the details of these patterns, however, are related to horizontal eddy viscosity models. Therefore, our focus will be given to the quantitative statistics of the dissipation level provided by each model.

To assess the performance of the proposed dynamic model, the probability density function (PDF) distributions of the estimated horizontal eddy viscosity coefficient v_e and the Smagorinsky constant c_S are computed in each physical setting. The statistically steady state data sets are collected between $t = 20$ and $t = 100$. For the dynamic Smagorinsky and
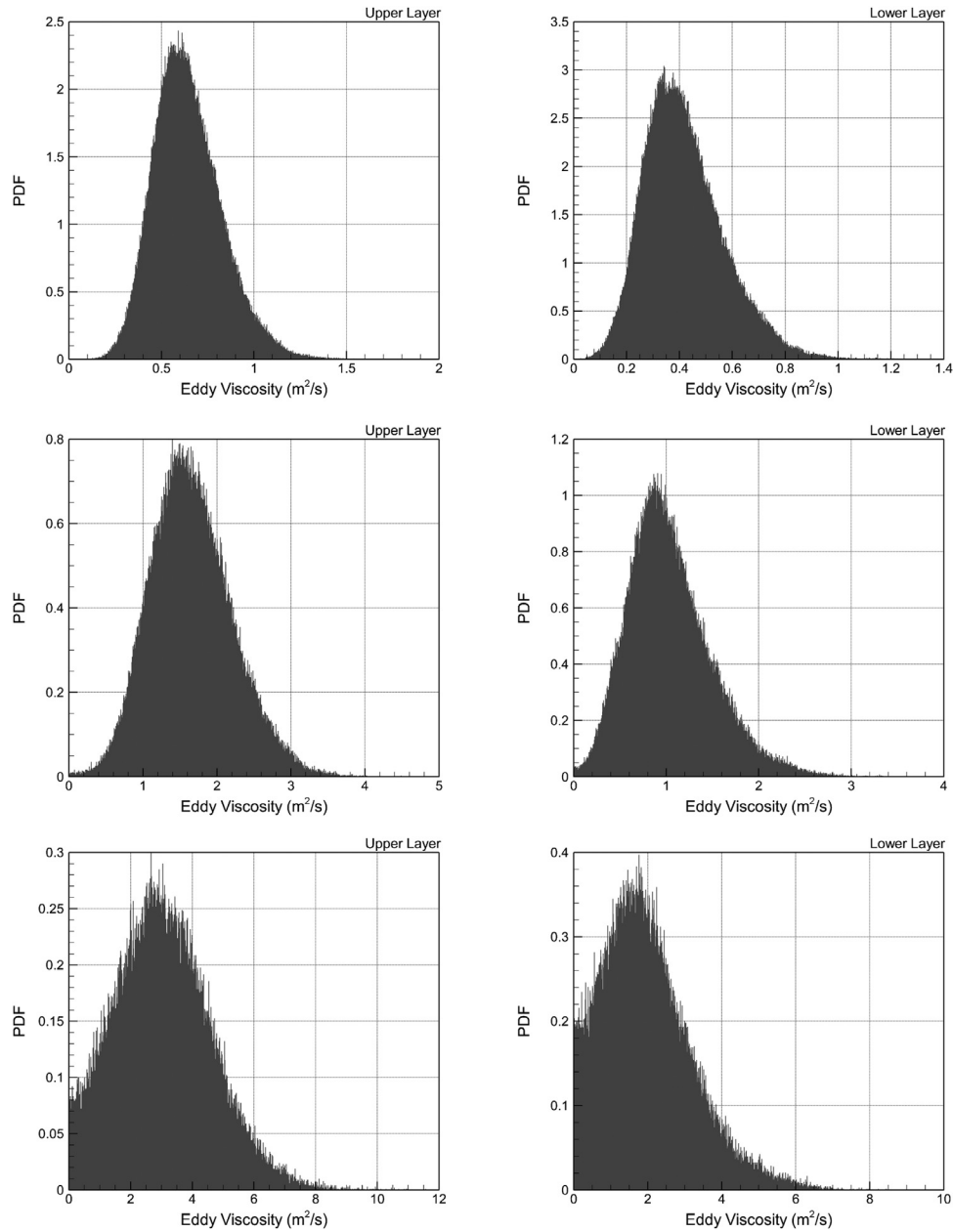
Fig. 20. Normalized probability density function (PDF) distributions of the eddy viscosity coefficient for the two-layer numerical experiments using the dynamic Leith model with resolutions of 512×512 (top row), 256×256 (middle row), and 128×128 (bottom row).

Leith models, Figs. 8 and 9, respectively, demonstrate the normalized PDF distributions for a set of numerical experiments varying the computational computational resolution for the case of Ro=0.0004. First of all, it is clear that the eddy viscosity increases with decreasing resolution. The dynamic models predict the eddy viscosity level between $\nu_e = 0$ and $\nu_e = 30$ m^2/s for the resolution of 256×512 and increases to a level between $\nu_e = 0$ and $\nu_e = 200$ m^2/s when we use a coarser resolution of 64×128. The dynamic Leith model shows slightly less dissipative behaviur compared to the dynamic Smagorinsky model due to its more scale selective nature. However, the PDF of c_S shows more universal behavior

showing a peak probability close to $c_S = 0.15$. We note that this prediction agrees well with a priori estimation based on the turbulence literature. However, it is also evident on examination of Fig. 9 that the dynamic coefficient of the Leith model varies between $c_L = 0.15$ and $c_L = 0.3$. A quantitative summary of the mean values (i.e., ensembled between $t = 20$ and $t = 100$) are also documented in Table 2 (for the dynamic Smagorinsky model) and Table 3 (for the dynamic Leith model). Performing the same type of analysis for Ro=0.0016, similar trends are shown in Figs. 10 and 11 confirming that the proposed dynamic model is robust with different ocean dynamics. Tables 4 and 5 also summarize our
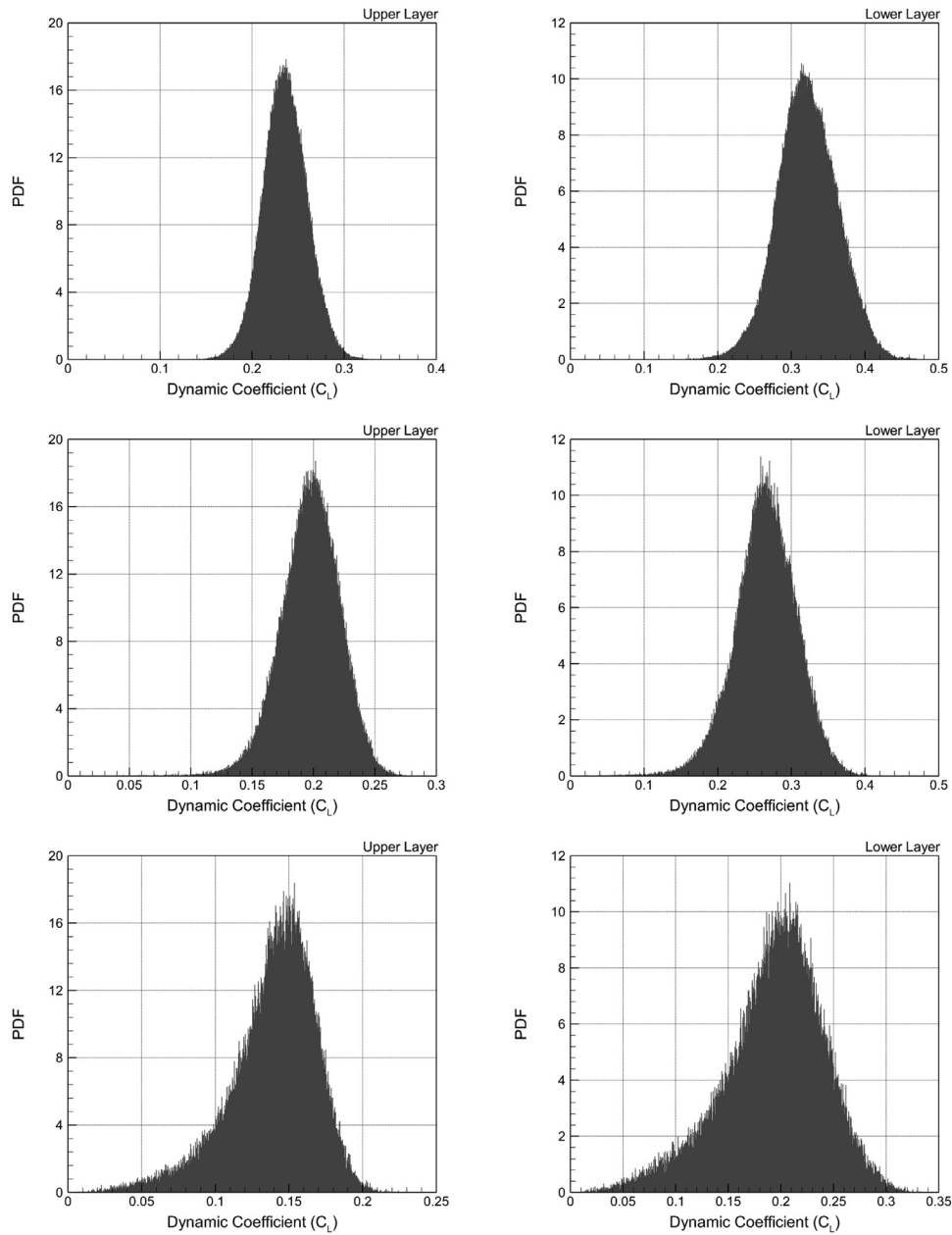
Fig. 21. Normalized probability density function (PDF) distributions of the dynamic coefficient for the two-layer numerical experiments using the dynamic Leith model with resolutions of 512×512 (top row), 256×256 (middle row), and 128×128 (bottom row).

findings for Ro=0.0016. It is also shown that an increase in the filtering ratio κ yields less amount of eddy viscosity for QG simulations.

Finally, we investigate numerically whether we can reproduce the four gyre time average circulation field by the proposed models. Using a set of resolutions of 64×128, 128×256, and 256×512, Fig. 12 displays the mean streamfunction contour plots obtained by using the dynamic Smagorinsky model for Ro = 0.0004. Solid and dashed lines in this figure represent counterclockwise and clockwise circulations, respectively. Fig. 13 provides the same data set for the dynamic Leith model. It can be easily seen that the four-

gyre mean circulation pattern can be reproduced by using the proposed anisotropic dynamic eddy viscosity parameterizations. Furthermore, the four-gyre pattern can also be reproduced by coarsening the resolution as shown in Figs. 12 and 13. The same analysis is presented in Figs. 14 and 15 for the case of Ro = 0.0016. It is clear that the dynamic modeling framework provided in Section 3 can provide a physical level of eddy viscosity coefficient varying spatially over the ocean basin, as well as varying in time, and can be used as a robust subgrid-scale parametrization in QG ocean models. It can be seen that the Leith model provides slightly less dissipative results.
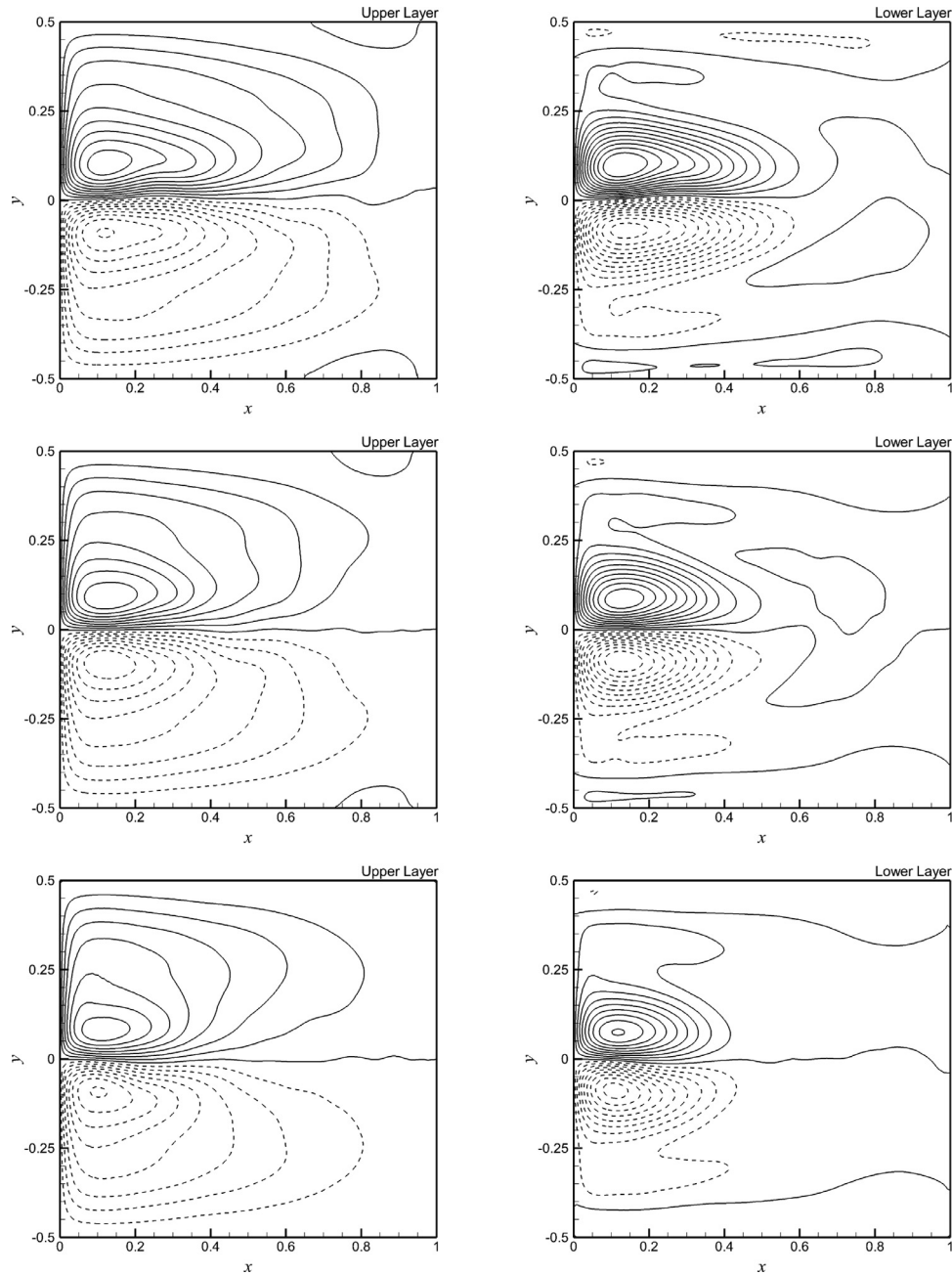
Fig. 22. Mean streamfunction contour plots for the two-layer numerical experiments using the dynamic Leith model with resolutions of 512×512 (top row), 256×256 (middle row), and 128×128 (bottom row). An equidistant contour interval of $\Delta \psi = 0.1$ is used.

5.2. Two-layer QG2 experiments

The main goal of this section is to test the proposed dynamic models in the numerical simulation of the two-layer QG model. We also investigate the sensitivity of the proposed dynamic models with respect to the filtering ratio κ. Following the same procedure presented in the previous subsection, we consider two different nonlinear viscosity kernels in conjunction with the proposed dynamic framework, namely, the dynamic Smagorinsky and Leith models. The two-layer numerical experiments presented here represent a moderate ocean basin with the physical parameters used by Ozgokmen

and Chassignet [71] and San et al. [83]. In terms of the classification given by Berloff and McWilliams [7], these sets of experiments lie under the chaotic regime. Further details of the two-layer QG dynamics can be found in [83]. The dimensionless parameters used in our simulations are $\delta = 0.2$, $\sigma = 5.74$, Fr=0.087, and Ro=0.00025. This setting corresponds to the physical parameters given as L=2000 km, H_1=1 km, H_2=4 km, f_0=9.35 $\times$ 10^{-5} s^{-1}, β=1.75 $\times$ 10^{-11} m^{-1} s^{-1}, g'=0.02 m s^{-2}, ρ_1=1030 kg m^{-3}, τ_0=0.1 N m^{-2}, γ=5.0 $\times$ 10^{-8} s^{-1}. The dimensionless computational domain is defined in $x \in [0, 1]$ and $y \in [-0.5, +0.5]$ using the double-gyre wind forcing stress given in Section 2.2.

Table 6
Dynamic Smagorinsky modeling of the two-layer experiment: mean values of the eddy viscosity coefficient and the Smagorinsky constant for the upper and lower layers (considering both space and time averaging).

| Filter ratio | 512×512 | | 256×256 | | 128×128 | |
	ν_e (m²/s)	c_S	ν_e (m²/s)	c_S	ν_e (m²/s)	c_S
The upper layer:						
$\kappa = 2$	1.16	0.16	3.67	0.13	8.32	0.11
$\kappa = \sqrt{6}$	0.67	0.096	1.76	0.083	4.15	0.069
$\kappa = 3$	0.27	0.055	0.75	0.049	1.72	0.037
The lower layer:						
$\kappa = 2$	0.87	0.16	2.81	0.16	8.17	0.15
$\kappa = \sqrt{6}$	0.32	0.092	1.05	0.090	3.13	0.084
$\kappa = 3$	0.14	0.058	0.45	0.057	1.29	0.051

Table 7
Dynamic Leith modeling of the two-layer experiment: mean values of the eddy viscosity coefficient and the Leith constant for the upper and lower layers (considering both space and time averaging).

| Filter ratio | 512×512 | | 256×256 | | 128×128 | |
	ν_e (m²/s)	c_L	ν_e (m²/s)	c_L	ν_e (m²/s)	c_L
The upper layer:						
$\kappa = 2$	0.65	0.23	1.65	0.20	3.04	0.14
$\kappa = \sqrt{6}$	0.15	0.12	0.35	0.09	0.66	0.06
$\kappa = 3$	0.04	0.06	0.08	0.05	0.21	0.04
The lower layer:						
$\kappa = 2$	0.42	0.32	1.03	0.26	1.96	0.19
$\kappa = \sqrt{6}$	0.14	0.21	0.37	0.17	0.83	0.14
$\kappa = 3$	0.06	0.14	0.15	0.12	0.40	0.10

Fig. 16 shows the time series of basin integrated kinetic energy in each layer. It can be seen that a quasi-stationary chaotic state is obtained after an initial transient period. We have collected data between $t = 2$ and $t = 10$ to assess the performance of the proposed subgrid-scale models. We note that the dimensionless time unit corresponds to 3.64 years providing approximately 30 years of data collection window in our two-layer experiments.

To quantify the effect of the numerical resolution, we perform our numerical experiments on a set of resolutions with 128^2, 256^2, and 512^2 grid points. Fig. 17 demonstrates the normalized PDF distributions of the provided eddy viscosity by the Smagorinsky model. We note that the PDF distribution represents both space and time variations (i.e., over the whole basin between $t = 2$ and $t = 10$). Because of the dynamic procedure to obtain eddy viscosity coefficients in each layer, the proposed model yields different eddy viscosity magnitudes in the upper and lower layers according to their flow characteristics. Since the upper layer is dynamically more active, the proposed dynamical model successfully provides higher eddy viscosity distribution in the upper layer. Fig. 18 displays the normalized PDF distribution of the associated dynamic coefficient c_S for upper and lower layers. It is clear that c_S varies between 0.1 and 0.2 which is agree well with the previous studies [28]. We have also seen that the variation of c_S is also resolution dependant, while yielding slightly higher values for higher resolutions. The results of the time-averaged mean streamfunction field data obtained in the statistically steady state are given in Fig. 19. The results show strong western boundary currents with cyclonic counter-clockwise rotating gyres and anticyclonic clockwise rotating gyres producing a strong eastward jet. We emphasize that the plot in Fig. 19 is similar to the mean streamfunction contour plots presented by Ozgokmen and Chassignet [71] and San et al. [83]. Figs. 20–22 illustrate same analysis by using the dynamic Leith model. A quantitative summary of the proposed models are presented in Tables 6 and 7 for the dynamic Smagorinsky and the dynamic Leith models, respectively. Although it follows the same trend, it is clear that the Leith model provides slightly less amount of subgrid-scale contribution to the mean flow dynamics. However, there is no significant difference between models, besides the fact that slightly less dissipative results can be obtained by using the Leith viscosity kernel. This can be attributed to the fact that the Leith model is more scale-selective than the Smagorinsky model because it depends on a higher derivative of velocity (e.g., see also [37]).

6. Conclusions

The horizontal eddy viscosity parameterization plays a crucial role in the dynamics of large scale ocean circulation problems because of the difference between the horizontal scale of the ocean basin and the effective scale of molecular diffusion. The associated eddy viscosity coefficient is much larger than the molecular viscosity since the advection by the velocity fluctuations acts much more rapidly to transport momentum than the molecular diffusion. Therefore, an impractically fine computational resolution is necessary if the ocean models were to resolve the full spectra of turbulence down to the Kolmogorov scale regarding the molecular viscosity coefficient of sea water. In the present study, a dynamic modeling framework is developed to compute the horizontal eddy viscosity coefficient used in the large-scale ocean circulation models. We use a second-order conservative Arakawa scheme for the spatial discretization and a third-order Runge–Kutta scheme for the temporal integration.

First, the method is applied to a wind-driven quasi-geostrophic four-gyre problem. The double-gyre wind forcing yields a four-gyre circulation pattern in statistically steady state and represents an ideal test problem to assess whether the dynamic model captures the four-gyre mean circulation pattern without using any a priori estimation for the eddy viscosity. Two physical settings were used to assess the performance of the dynamic model for various resolutions in these one-layer numerical experiments. We showed that the large scale quasigeostrophic dynamics are well captured by the proposed model even with small resolutions. The main advantages of the dynamic model are that it can easily adjust the level of eddy viscosity coefficient from the local structure of the flow, it is clear as a physical concept and easy to be implemented in general circulation models. An increase

in the resolution adaptively results in a decrease in the level of eddy viscosity and the four-gyre structure patterns of the time-averaged streamfunction contour plots are recovered by the proposed dynamic model in each resolution. Indeed, we emphasize that the mean four-gyre circulation pattern is simply the nature of beta and wind stress curl effects. However, we show that the details of these gyres are related to horizontal eddy viscosity models. Therefore, we present a quantitative data set on the level of horizontal eddy viscosity coefficient with respect to the free modeling parameters.

Next, the proposed models are extended to solve the two-layer quasigeostrophic equations. Our computations show that the large scale stratified QG ocean dynamics are well captured by the proposed model without using any a priori estimation for the eddy viscosity. The main advantage of the proposed dynamic model is that it puts forth a flexible framework and can easily adjust the magnitude of the eddy viscosity coefficient in each layer from the local structure of the flow using various viscosity forms like the Smagorisnky and Leith models tested in the present work.

In all of the numerical experiments we compute the probability density functions for the horizontal eddy viscosity coefficient and the dynamic modeling constant and determine their mean values. It is shown that the self-adaptive value of the Smagorinsky constant shows more universal behaviur with respect to change in resolution and varies between 0.12 and 0.18 in both one- and two-layer experiments, which is in agreement with previously reported values in LES literature. However, the dynamic Leith constant varies between 0.14 and 0.25. By comparing the Smagorinsky and Leith models, we find that the dynamic Leith model provides a lower amount of eddy viscosity production over the whole ocean basins. This first step in the numerical assessment of the dynamic modeling of horizontal eddy viscosity coefficient demonstrates that the proposed framework represents a viable subgrid-scale parametrization for more complicated general circulation models.

References

[1] U. Achatz, U. Löbl, S.I. Dolaptchiev, A. Gritsun, J. Atmos. Sci. 70 (6) (2013) 1833–1846.
[2] A. Arakawa, J. Comput. Phys. 1 (1) (1966) 119–143.
[3] E. Awad, E. Toorman, C. Lacor, J. Mar. Syst. 77 (2009) 511–528.
[4] M. Bates, R. Tulloch, J. Marshall, R. Ferrari, J. Phys. Oceanogr. 44 (6) (2014) 1523–1540.
[5] P. Berloff, I. Kamenkovich, J. Pedlosky, J. Fluid Mech. 628 (2009) 395–425.
[6] P. Berloff, S.P. Meacham, J. Phys. Oceanogr. 28 (2) (1998) 361–388.
[7] P.S. Berloff, J.C. McWilliams, J. Phys. Oceanogr. 29 (8) (1999) 1925–1949.
[8] P.S. Berloff, S.P. Meacham, J. Mar. Res. 55 (3) (1997) 407–451.
[9] L. Berselli, T. Iliescu, W.J. Layton, Mathematics of Large Eddy Simulation of Turbulent Flows, Springer-Verlag, 2006.
[10] G. Boer, T. Shepherd, J. Atmos. Sci. 40 (1) (1983) 164–184.
[11] T. Brandt, Int. J. Numer. Methods Fluids 51 (6) (2006) 635–657.
[12] K. Bryan, J. Atmos. Sci. 20 (6) (1963) 594–606.
[13] J.-M. Campin, C. Hill, H. Jones, J. Marshall, Ocean Model. 36 (2011) 90–101.
[14] Q. Chen, M. Gunzburger, T. Ringler, Mon. Weather Rev. 139 (8) (2011) 2614–2629.
[15] F.K. Chow, R.L. Street, J. Appl. Meteorol. Climatol. 48 (5) (2009) 1050–1065.
[16] P.F. Cummins, J. Mar. Res. 50 (4) (1992) 545–566.
[17] B. Cushman-Roisin, J.-M. Beckers, Introduction to Geophysical Fluid Dynamics: Physical and Numerical Aspects, Academic Press, 2011.
[18] J.W. Deardorff, J. Fluid Mech. 41 (1970) 453–480.
[19] M.T. DiBattista, A.J. Majda, Theor. Comput. Fluid Dyn. 14 (5) (2001) 293–322.
[20] P.A. Dirmeyer, B.A. Cash, J.L. Kinter III, T. Jung, L. Marx, M. Satoh, C. Stan, H. Tomita, P. Towers, N. Wedi, Clim. Dyn. 39 (2012) 399–418.
[21] E. Fedorovich, R. Conzemius, D. Mironov, J. Atmos. Sci. 61 (2004a) 281–295.
[22] E. Fedorovich, R. Rotunno, B. Stevens, Atmospheric Turbulence and Mesoscale Meteorology: Scientific Research Inspired by Doug Lilly, Cambridge University Press, 2004b.
[23] R.O. Fox, Annu. Rev. Fluid Mech. 44 (2012) 47–76.
[24] B. Fox-Kemper, G. Danabasoglu, R. Ferrari, S.M. Griffies, R.W. Hallberg, M.M. Holland, M.E. Maltrud, S. Peacock, B.L. Samuels, Ocean Model. 39 (1) (2011) 61–78.
[25] B. Fox-Kemper, D. Menemenlis, in: M. Hecht, H. Hasum (Eds.), Ocean Modeling in an Eddying Regime, Geophysical Monograph Series, Vol. 177, American Geophysical Union, Washington, DC, 2008, pp. 319–338.
[26] J.S. Frederiksen, T.J. O'Kane, M.J. Zidikheri, Phys. Scr. 85 (6) (2012) 068202.
[27] J.S. Frederiksen, T.J. O'Kane, M.J. Zidikheri, Philos. Trans. R. Soc. Lond. A: Math. Phys. Eng. Sci. 371 (2013) 20120166.
[28] B. Galperin, Large Eddy Simulation of Complex Engineering and Geophysical Flows, Cambridge University Press, 1993.
[29] W.L. Gates, J. Atmos. Sci. 25 (1968) 3–22.
[30] M. Germano, U. Piomelli, P. Moin, W.H. Cabot, Phys. Fluids 3 (1991) 1760–1766.
[31] S. Ghosal, T.S. Lund, P. Moin, K. Akselvoll, J. Fluid Mech. 286 (1) (1995) 229–255.
[32] A.E. Gill, Atmosphere-Ocean Dynamics, Academic Press, 1982.
[33] S. Gottlieb, C.-W. Shu, Math. Comput. 67 (221) (1998) 73–85.
[34] S. Gottlieb, C.-W. Shu, E. Tadmor, SIAM Rev. 43 (1) (2001) 89–112.
[35] R.J. Greatbatch, B.T. Nadiga, J. Phys. Oceanogr. 30 (6) (2000) 1461–1471.
[36] S.M. Griffies, C. Böning, F.O. Bryan, E.P. Chassignet, R. Gerdes, H. Hasumi, A. Hirst, A.-M. Treguier, D. Webb, Ocean Model. 2 (2000) 123–192.
[37] S.M. Griffies, R.W. Hallberg, Mon. Weather Rev. 128 (8) (2000) 2935–2946.
[38] S. Hagemann, L.D. Gates, Clim. Dyn. 21 (3–4) (2003) 349–359.
[39] R. Hallberg, Ocean Model. 72 (2013) 92–103.
[40] W.R. Holland, J. Phys. Oceanogr. 8 (3) (1978) 363–392.
[41] W.R. Holland, L.B. Lin, J. Phys. Oceanogr. 5 (4) (1975) 642–657.
[42] D.D. Holm, B.T. Nadiga, J. Phys. Oceanogr. 33 (2003) 2355–2365.
[43] T.J. Hughes, L. Mazzei, A.A. Oberai, A.A. Wray, Phys. Fluids 13 (2001) 505–512.
[44] M.F. Jansen, A.J. Adcroft, R. Hallberg, I.M. Held, Ocean Model. 92 (2015a) 28–41.
[45] M.F. Jansen, I.M. Held, Ocean Model. 80 (2014) 36–48.
[46] M.F. Jansen, I.M. Held, A. Adcroft, R. Hallberg, Ocean Model. 94 (2015b) 15–26.
[47] S. Jiang, F.-F. Jin, M. Ghil, J. Phys. Oceanogr. 25 (5) (1995) 764–786.
[48] E. Kaas, A. Guldberg, W. May, M. Déqué, Tellus A 51 (5) (1999) 612–629.
[49] K.A. Kelly, R.J. Small, R. Samelson, B. Qiu, T.M. Joyce, Y.-O. Kwon, M.F. Cronin, J. Clim. 23 (21) (2010) 5644–5667.
[50] V. Kitsios, J.S. Frederiksen, M.J. Zidikheri, J. Atmos. Sci. 69 (4) (2012) 1427–1445.
[51] J.N. Koshyk, G.J. Boer, J. Atmos. Sci. 52 (7) (1995) 965–976.
[52] C. Leith, Physica D 98 (2) (1996) 481–491.
[53] C.E. Leith, Phys. Fluids 11 (1968) 671–672.

[54] M. Lesieur, O. Metais, Annu. Rev. Fluid Mech. 28 (1996) 45–82.
[55] D.K. Lilly, Phys. Fluids 4 (1992) 633–634.
[56] D.P. Marshall, J.R. Maddison, P.S. Berloff, J. Phys. Oceanogr. 42 (4) (2012) 539–557.
[57] J. Marshall, C. Hill, L. Perelman, A. Adcroft, J. Geophys. Res.: Oceans 102 (C3) (1997) 5733–5752.
[58] J.C. McWilliams, Fundamentals of Geophysical Fluid Dynamics, Cambridge University Press, 2006.
[59] T.T. Medjo, SIAM J. Numer. Anal. 37 (6) (2000) 2005–2022.
[60] D. Menemenlis, C. Hill, A. Adcroft, J. Campin, B. Cheng, B. Ciotti, I. Fukumori, A. Koehl, P. Heimbach, C. Henze, et al., NASA Supercomputer Improves Prospects for Ocean Climate Research, American Geophysical Union, 2005.
[61] C. Meneveau, J. Katz, Annu. Rev. Fluid Mech. 32 (1) (2000) 1–32.
[62] R.N. Miller, Numerical Modeling of Ocean Circulation, Cambridge University Press, 2007.
[63] P.K. Mishra, J. Herault, S. Fauve, M.K. Verma, Phys. Rev. E 91 (2015) 053005.
[64] C.-H. Moeng, J. Atmos. Sci. 41 (1984) 2052–2062.
[65] P. Moin, Int. J. Heat Fluid Flow 23 (5) (2002) 710–720.
[66] P. Moin, Fundamentals of Engineering Numerical Analysis, Cambridge University Press, 2010.
[67] J.S. Mullen, P.F. Fischer, Commun. Numer. Methods Eng. 15 (1) (1999) 9–18.
[68] B.T. Nadiga, L.G. Margolin, J. Phys. Oceanogr. 31 (8) (2001) 2525–2531.
[69] F.M. Najjar, D.K. Tafti, Phys. Fluids 8 (1996) 1076–1088.
[70] J.J. Nauw, H.A. Dijkstra, E. Simonnet, J. Mar. Res. 62 (5) (2004) 684–719.
[71] T.M. Özgökmen, E.P. Chassignet, J. Phys. Oceanogr. 28 (3) (1998) 461–484.
[72] J. Pedlosky, Geophysical Fluid Dynamics, Springer, 2013.
[73] U. Piomelli, Prog. Aerosp. Sci. 35 (4) (1999) 335–362.
[74] H. Pitsch, Annu. Rev. Fluid Mech. 38 (2006) 453–482.
[75] F. Porté-Agel, M.B. Parlange, C. Meneveau, W.E. Eichinger, J. Atmos. Sci. 58 (18) (2001) 2673–2698.
[76] W.H. Press, B.P. Flannery, S.A. Teukolsky, W.T. Vetterling, Numerical Recipes in FORTRAN, Cambridge University Press, 1992.
[77] T. Ringler, M. Petersen, R.L. Higdon, D. Jacobsen, P.W. Jones, M. Maltrud, Ocean Model. 69 (2013) 211–232.
[78] P. Sagaut, Large Eddy Simulation for Incompressible Flows: An Introduction, Springer-Verlag, 2006.
[79] P. Sagaut, R. Grohens, Int. J. Numer. Methods Fluids 31 (8) (1999) 1195–1220.
[80] O. San, Int. J. Comput. Fluid Dyn. 28 (2014) 363–382.
[81] O. San, A.E. Staples, Comput. Fluids 63 (2012) 105–127.
[82] O. San, A.E. Staples, Int. J. Multiscale Comput. Eng. 11 (2013) 463–495.
[83] O. San, A.E. Staples, T. Iliescu, Ocean Model. 63 (2013) 1–20.
[84] O. San, A.E. Staples, Z. Wang, T. Iliescu, Ocean Model. 40 (2) (2011) 120–132.
[85] J. Shen, T.T. Medjo, S. Wang, J. Comput. Phys. 155 (2) (1999) 387–409.
[86] S. Singh, D. You, Int. J. Heat Fluid Flow 42 (2013) 94–104.
[87] J. Smagorinsky, Mon. Weather Rev. 91 (3) (1963) 99–164.
[88] P.R. Spalart, Annu. Rev. Fluid Mech. 41 (2009) 181–202.
[89] R. Stoll, F. Porté-Agel, Bound.-Layer Meteorol. 126 (1) (2008) 1–28.
[90] H. Stommel, The Gulf Atream: A Physical and Dynamical Description, University of California Press, Berkeley, CA, 1972.
[91] P. Sura, K. Fraedrich, F. Lunkeit, J. Phys. Oceanogr. 31 (2) (2001) 411–426.
[92] Y. Tanaka, K. Akitomo, J. Oceanogr. 66 (4) (2010) 475–487.
[93] G.K. Vallis, Atmospheric and Oceanic Fluid Dynamics: Fundamentals and Large-Scale Circulation, Cambridge University Press, 2006.
[94] O.V. Vasilyev, T.S. Lund, P. Moin, J. Comput. Phys. 146 (1) (1998) 82–104.
[95] M. Visbeck, J. Marshall, T. Haine, M. Spall, J. Phys. Oceanogr. 27 (3) (1997) 381–402.
[96] C. Wagner, T. Hüttl, P. Sagaut, Large-Eddy Simulation for Acoustics, vol. 20, Cambridge University Press, 2007.
[97] D. You, P. Moin, Phys. Fluids 19 (2007) 065110.